Department of Physics and Astronomy
University of Heidelberg

Master Thesis in Physics
submitted by

Jonas Karthein

born in Saarbrücken (Germany)

2017

Precision mass measurements using the Phase-Imaging Ion-Cyclotron-Resonance detection technique

This Master thesis has been carried out by Jonas Karthein
at the
Conseille Européen pour la Recherche Nucléaire (CERN)

under the supervision of

Prof. Dr. rer. nat. Klaus Blaum
(Max-Planck-Institut für Kernphysik (MPIK))

and

Dr. rer. nat., apl. Prof. Yuri Litvinov
(GSI Helmholtzzentrum für Schwerionenforschung)

Abstract

This thesis presents the implementation and improvement of the Phase-Imaging Ion-Cyclotron-Resonance (PI-ICR) detection technique at the ISOLTRAP experiment, located at the ISOLDE / CERN, with the purpose of on-line high-precision and high-resolution mass spectrometry. Extensive simulation studies were performed with the aim of improving the phase-imaging resolution and finding the optimal position for detector placement. Following the outcome of these simulations, the detector was moved out of a region of electric-field distortion and closer to the center of the Penning trap, showing a dramatic improvement in the quality and reproducibility of the phase-imaging measurements. A new image reconstitution and analysis software for the MCP-PS detector was written in Python and ROOT and introduced in the framework of PI-ICR mass measurements. The state of the art in the field of time-of-flight ion-cyclotron-resonance measurements is illustrated through an analysis of on-line measurements of the mirror nuclei ^{21}Na/Ne and ^{23}Mg/Na using the Ramsey excitation pattern. The Q-values determined from this analysis play an important role for verifying the Conserved-Vector-Current hypothesis and for testing the unitarity of the CKM quark-mixing matrix. Finally, the results of a first high-precision, on-line measurement using the PI-ICR technique are presented, addressing the Q-value of the ^{88}Rb-^{88}Sr β-decay.

Kurzfassung

Diese Arbeit präsentiert die Implementierung und Verbesserungen der "Phase-Imaging Ion-Cyclotron-Resonance" (PI-ICR) Detektionstechnik am ISOLTRAP-Experiment an ISOLDE / CERN in Hinblick auf Hochpräzissionsmassenspektrometrie, sowie deren erste Online-Ergebnisse. Ausführliche Simulationen wurden mit dem Ziel durchgeführt, die Phasenbildauflösung zu vergrößern und eine optimale Detektorposition zu finden. Als Ergebnis dieser Studien wurde der Detektor aus einem Bereich mit starken, elektrischen Streupotenzialen näher zum Fallenzentrum hin versetzt. Dies führte zu einer signifikanten Verbesserung der PI-ICR Messungen sowie zur Reproduzierbarkeit von optimalen Potentialparametern. Zudem wurde eine neue Bildrekonstruktions- und Analysesoftware für PI-ICR-Messungen in Python und ROOT geschrieben. Die bisher für Hochpräzisionsmassenmessung an kurzlebigen Nukliden am weitesten verbreitete Methode (die "Time-of-Flight Ion-Cyclotron-Resonance" (ToF-ICR) Detektionstechnik mit Ramsey-Anregungsschema) wird im Rahmen einer Analyse von Onlinemessungen der Spiegelkerne ^{21}Na/Ne und ^{23}Mg/Na vorgestellt. Der Q-Wert dieser Zerfälle spielt eine wichtige Rolle bei der Überprüfung der Vektorstrom-Erhaltungshypothese (*engl. Conserved-Vector-Current hypothesis*). Außerdem können die neu gewonnen Ergebnisse für den Unitaritätstest der Cabibbo-Kobayashi-Maskawa (CKM) Quarkmischungsmatrix herangezogen werden. Zusätzlich werden erste Hochpräzisionsmassenmessungen mittels PI-ICR an online erzeugten, radioaktiven Isotopen vorgestellt. Hierbei wurde der Q-Wert des ^{88}Rb-^{88}Sr-β-Zerfalls bestimmt und mit Literatur- sowie ToF-ICR-Messwerten verglichen.

Contents

List of Figures

List of Tables

List of abbreviations

PI-ICR Phase-imaging ion-cyclotron-resonance technique

CERN Conseille Européen pour la Recherche Nucléaire

MPIK Max-Planck-Institut für Kernphysik

ISOLDE Isotope separator online device

MCP Micro-channel plate detector

MCP-PS Position-sensitive micro-channel plate detector

ToF-ICR Time-of-flight ion-cyclotron-resonance detection technique

MR-ToF-MS Multi-reflection time-of-flight mass spectrometer/separator

UT Upper trap

GUI Graphical user interface

AME16 Atomic-mass evaluation 2016

AC Alternating current

P1/2 Pattern 1/2

C Center

HV High-voltage

LHC Large hadron collider

Linac Linear accelerator

PSB Proton synchrotron booster

PS Proton synchrotron

SPS Super proton synchrotron

GPS General purpose separator

HRS High-resolution separator

RFQ Radio-frequency quadrupole trap

CVC Conserved vector current

CKM Cabibbo-Kobayashi-Maskawa matrix

FWHM Full width at half maximum

MEAS Measurement ion

REF Reference ion

Introduction

Mass separation techniques using ion traps are becoming integral parts of all low-energy nuclear physics facilities worldwide. While for many years their application has been restricted to mass measurements of exotic nuclides, there is an increasing demand of ion traps as general-purpose mass separators for a wide range of applications. Recently [1, 2], with the advances in fast-response position-sensitive detectors, a new ion measurement technique has become possible, achieving the spatial separation of ion species of different masses by exploiting their different cyclotron frequencies in a Penning trap. With a separation power up to 10^6 for a trapping time of only 100 ms, this so-called phase-imaging ion-cyclotron-resonance (PI-ICR) technique makes it feasible to produce high-resolution mass spectra for beam analysis, ion counting applications and mass measurements, or pure beams of short-lived nuclear isomers, for subsequent nuclear-physics studies by complementary techniques. The ability to not only separate and purify but also identify short-lived and close-lying isomers becomes crucial in the context of nuclear-physics studies at the next-generation radio-active-ion-beam facilities, which will move predominantly in the sub-100-ms half-life range.

This work addresses the final implementation phase of the PI-ICR detection technique at the ISOLTRAP experiment at CERN. By construction the ISOLTRAP setup possesses a number of particularities which do not affect the until-now standard mass measurement technique (the time-of-flight ion-cyclotron resonance), but are crucial with respect to both the quality of the ion-phase imaging as well as the accuracy of phase determination. When this work started, a number of ion-optical problems were still plaguing PI-ICR measurements, which are reflected in large and distorted spots on the position sensitive detector as well as unreproducible optimal transport-potential settings. Moreover there was no flexible and automated software for data analysis. The PI-ICR detection technique at ISOLTRAP had also neither been proven yet to be able to achieve a precision and accuracy comparable (or superior) to the well-established TOF-ICR measurements nor been operational for on-line usage.

To summarize, this thesis covers the resolution of the mentioned hardware and software issues and presents the successful implementation of the PI-ICR detection technique with the result of the first high-precision, on-line measurement, addressing the Q-value of the ^{88}Rb-^{88}Sr β-decay. In addition, the state of the art in the field of time-of-flight ion-cyclotron-resonance measurements is illustrated through an analysis of on-line measurements of the

mirror nuclei ^{21}Na/Ne and ^{23}Mg/Na using the Ramsey excitation pattern. The Q-values determined from this analysis play an important role for verifying the Conserved-Vector-Current hypothesis and for testing the unitarity of the CKM quark-mixing matrix.

1 Storing charged particles

In this chapter the ion traps and corresponding ion dynamics relevant for the subject of this thesis will be discussed. The summary is not complete, therefore the inquisitive reader can find additional information in the treaty [3] or in the lecture on Stored Charged Particles of Prof. Dr. K. Blaum [4] which were the bibliographical basis for this chapter.

1.1 Penning trap

Defined in simple terms, an ion trap is any device which confines the motion of an ion in a limited volume of space. As a consequence of Gauss' Law an ion within its rest frame can not be trapped in three dimensions just by electrostatic potentials. Therefore one simple solution for an ion trap setup is a combination of a magnetic-dipolar and an electrostatic-multipolar field. Here, the magnetic field confines the ion in a radial plane and the electrostatic potential in the axial direction.
The mass spectrometer ISOLTRAP, where the research presented here took place, is comprised of two Penning traps. Hence this section introduces the theoretical principles of ion storage in a Penning trap. An extensive description of an ion in a Penning trap can be found in the review articles of L.S. Brown and G. Gabrielse [5], G. Bollen [6] as well as K. Blaum [7] where emphasis is on mass determination.

1.1.1 Motion in a Penning trap

In a magnetic field, an ion with charge q and mass m moves with the cyclotron frequency ω_c

$$\omega_c = \frac{q}{m}B \tag{1.1}$$

on an orbit around the magnetic field lines. This leads to a trapping in the radial plane perpendicular to the magnetic field lines which is taken along the z-axis. If one now overlaps the magnetic field with an electrostatic quadrupolar potential $V(z,\rho)$

$$V(z,\rho) = \frac{V_0}{2d^2}\left(z^2 - \frac{\rho^2}{2}\right) \tag{1.2}$$

one gets a trapping in all dimensions. Here, z and ρ are the polar coordinates. Such a potential can be achieved by a combination of three rotational hyperboloids (one ring electrode and two end caps, see Fig. 1.1 left) or by a combination of cylindrical electrodes (a ring, two

end caps and several correction electrodes, see Fig. 1.1 right).

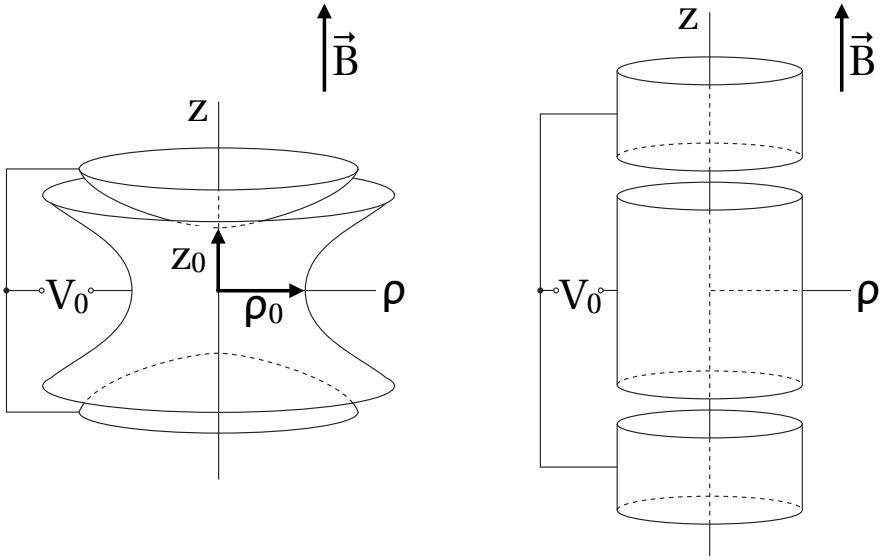

Figure 1.1: Hyperbolic (left) vs. cylindric Penning trap (right). The magnetic field is in both cases along the trap axis z. For details, see text. [4]

Both variants are implemented at ISOLTRAP and will be shown in Sec. 2.3. V_0 is the applied potential between the ring electrode and the two end cap electrodes. For a hyperbolic Penning trap, ρ_0 is the minimal distance between the center and the edge of the ring electrode, while z_0 is the distance between the end caps and the trap center. The dimension d of the trap is then given by

$$d^2 = \frac{1}{2}\left(z_0^2 + \frac{\rho_0^2}{2}\right). \tag{1.3}$$

If one now solves the equations of motion [5] in space

$$m\ddot{z} = qE_z \qquad \text{and} \qquad m\ddot{\vec{\rho}} = q\left(\vec{E}_\rho + \dot{\vec{\rho}} \times \vec{B}\right) \tag{1.4}$$

with the electrical field strength

$$E_z = -\frac{V_0}{d^2}z \qquad \text{and} \qquad \vec{E}_\rho = \left(\frac{V_0}{2d^2}\right)\vec{\rho} \tag{1.5}$$

one obtains the equation of motion of a trapped ion. This motion consists of three eigen motions (see Fig. 1.2) — one axial motion ν_z and two radial ones ω_+ and ω_-:

$$\omega_z = \sqrt{\frac{qV_0}{md^2}} \qquad \text{and} \qquad \omega_\pm = \frac{\omega_c}{2} \pm \sqrt{\frac{\omega_c^2}{4} - \frac{\omega_z^2}{2}}. \tag{1.6}$$

Note that $\nu_i = \omega_i/2\pi$. The axial harmonic frequency ω_z is only dependent on the applied trapping potential V_0 and the dimension parameter d. The radial frequencies ω_+, also known as modified cyclotron frequency, and ω_-, known as magnetron frequency, can be expressed via a series expansion of the radial eigen frequencies to:

$$\omega_- \approx \frac{V_0}{2d^2B} \qquad \text{and} \qquad \omega_+ \approx \omega_c - \frac{V_0}{2d^2B}. \tag{1.7}$$

So in first order the magnetron frequency is mass independent. For the eigen frequencies in an ideal Penning trap these relations follow:

$$\omega_c = \omega_+ + \omega_- \tag{1.8}$$

$$\omega_c^2 = \omega_+^2 + \omega_-^2 + \omega_z^2 \tag{1.9}$$

$$\omega_z^2 = 2\omega_+\omega_- \ . \tag{1.10}$$

Table 1.1 shows typical values for each eigen frequency for different masses, but in general a simple relation can be found:

$$\omega_c > \omega_+ > \omega_z > \omega_-. \tag{1.11}$$

A scheme and detailed trajectory of the ion motion in the Penning trap is plotted in Fig. 1.2.

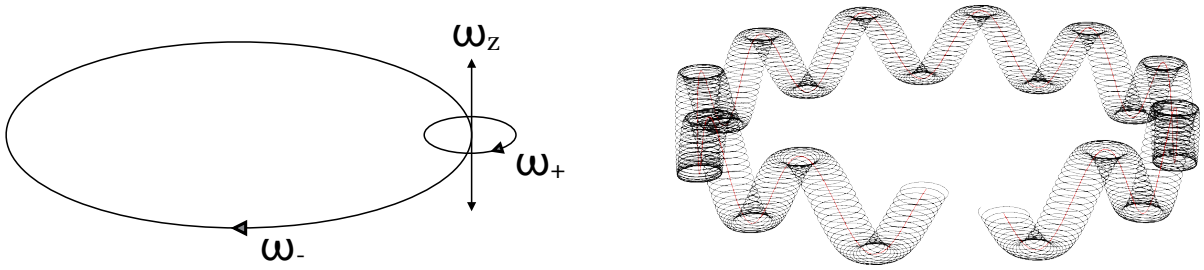

Figure 1.2: Schematic overview over the three eigen motions of a trapped ion inside a Penning trap. The left figure shows the motions separated where ω_- represents the magnetron motion, ω_z the axial motion and ω_+ the modified cyclotron motion. The right figure shows the superposition of the three eigen motions [8].

Table 1.1: Eigen frequencies of singly-charged ions of different mass trapped in a hyperbolic Penning trap with typical parameters: $\rho_0 = 13.0\,\text{mm}$, $z_0 = 11.18\,\text{mm}$, $V_0 = 10\,\text{V}$, $B = 5.9\,\text{T}$

A / u	**21**	**85**	**133**
ν_+	4337 kHz	1071 kHz	684 kHz
ν_z	107 kHz	54 kHz	43 kHz
ν_-	1 kHz	1 kHz	1 kHz
ν_c	4338 kHz	1072 kHz	685 kHz

1.1.2 Excitation of ion motions

Two different types of excitation schemes will be discussed, the first one is a dipolar excitation at resonance frequency which leads to an increase or decrease of the amplitude of that specific eigen frequency. The second type is quadrupolar excitation which allows shifting energies between the eigen motions.

Dipolar excitation

In order to manipulate one single eigen motion one radiates the trapped ion with a dipolar electrical field $\vec{E}_x$ with the radial component x

$$\vec{E}_x = \frac{U_d}{a} \cdot \cos(\omega_{rf} t - \phi_{rf}) \cdot \hat{x} \tag{1.12}$$

with an amplitude U_d at a radius a, the frequency ω_{rf} and the phase ϕ_{rf}. The radial field distribution can be achieved by segmenting the ring electrode with the dipolar excitation voltage applied on two opposing segments. It is also possible to manipulate the axial motion, here the voltage is just applied to the end caps. In order to achieve an ion response, the frequency of the excitation must be the eigen frequency of that motion. The dipolar excitation can be used to increase or decrease the amplitude / radius of the motion – depending on the phase relation of the particle's eigen motion and the applied field [9]. A particular application is to increase the radius of a contaminating ion species until it is removed from the trap.

Quadrupolar excitation

In order to couple two eigen motions of a trapped particle a quadrupolar excitation at the sum of their eigen frequencies is applied. This is possible by segmenting the ring electrode into four pieces and applying a field with the same phase on opposing segments and opposite phase on neighboring segments. This method can be also used for the mass determination, exploiting the fact that the cyclotron frequency is the sum of the two radial eigen frequencies $\omega_c = \omega_+ + \omega_-$ (see Eq. (1.8)). The applied electrical fields with radial components x and y have the following expression:

$$\vec{E}_x = \frac{2U_d}{a^2} \cdot \cos(\omega_{rf} t - \phi_{rf}) \cdot y\hat{x}, \tag{1.13}$$

$$\vec{E}_y = \frac{2U_d}{a^2} \cdot \cos(\omega_{rf} t - \phi_{rf}) \cdot x\hat{y}. \tag{1.14}$$

In the case of coupling the two radial motions with the resonant frequency $\omega_{rf} = \omega_c$ this leads to a full periodic conversion between the two motions, of radii ρ_+ and ρ_- [10, 11]. Figure 1.3 shows the simulated evolution of the radii for a conversion from pure magnetron to pure modified cyclotron motion.

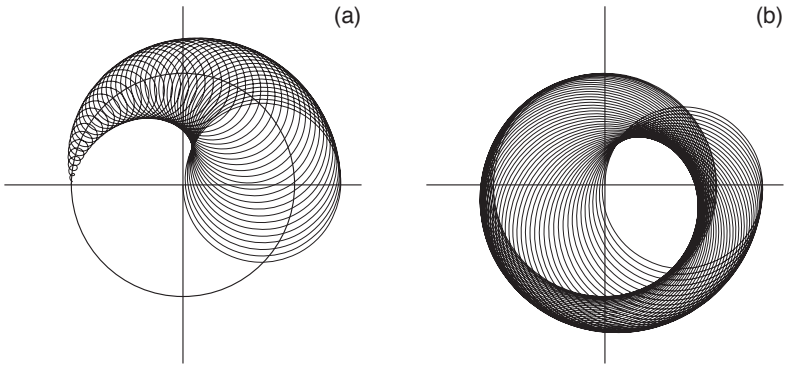

Figure 1.3: Conversion of a pure magnetron motion into pure cyclotron motion using an azimuthal quadrupolar field at the cyclotron frequency $\omega_c = \omega_+ + \omega_-$. An image of the ion trajectory in the early stage (left) and the late stage (right) of the conversion is shown. The cross-haired circle in the left picture shows the initial magnetron radius. [4, 6] Typical radii are ~ 0.7 mm in case of ISOLTRAP.

1.1.3 Penning-trap mass determination

This section deals with the two Penning-trap measurement and detection schemes used for short-lived isotopes at ISOLTRAP (see also Ch. 2.3). The first is the Time-of-Flight Ion-Cyclotron-Resonance (ToF-ICR) detection technique being used at ISOLTRAP for the last 30 years. The second one is the recently-developed Phase-Imaging Ion-Cyclotron-Resonance (PI-ICR) detection technique [1, 2, 12]. The latter has a clear advantage in achievable mass resolution and measurement time, in required statistics and the ability to spatially separate even close-lying isomeric states < 100 eV or isobars within the trap. In both methods the mass is determined by measuring the cyclotron frequency while the ion is detected destructively.

ToF-ICR: single pulse

In this method the cyclotron frequency is determined by measuring the ion's response to a quadrupolar excitation. To perform this measurement, the time of flight (ToF) of the ion from the trap to a detector – typically an MCP or Channeltron – is measured while scanning the frequency ω_{rf} of the irradiated quadrupolar field.
The measurement contains a sequence of steps. After the transport of the ion into the Penning trap the magnetron radius ρ_- is increased by a dipolar excitation at the corresponding frequency. Since ω_- is mass independent in first order the frequency doesn't need to be known very precisely. In the next step a quadrupolar conversion pulse (from now on called π-pulse) is applied, performing a simultaneous reduction of the magnetron radius and an increase of the cyclotron radius. For a certain combination of excitation time and amplitude, the magnetron radius is reduced to zero, while the cyclotron radius is increased from zero to a value equal to the initial magnetron radius. This is called the conversion process. The degree of conversion is determined by the deviation of the excitation frequency to the ion's real cyclotron frequency. Finally the ion is extracted and passes a magnetic field gradient to

the detector. Due to the resulting force

$$\vec{F} = -\vec{\mu}\left(\vec{\nabla}\vec{B}\right) = -\frac{E_r}{B}\frac{\partial B}{\partial z}\hat{e}_z \tag{1.15}$$

the radial kinetic energy E_r is converted into kinetic axial energy, therefore the ToF of ions at $\omega_{rf} = \omega_c$ (when the radial energy is maximal) is minimal. If ω_{rf} is varied around ω_c one obtains the typical ion-cyclotron resonance plot shown in Fig. 1.5 (left) for ^{23}Na (see also Ch. 3). The reason for the Sinc^2 shape derives from the rectangular envelope of the excitation pulse in the time domain (see Fig. 1.4). In the frequency domain a rectangular time pattern is transformed into a Sinc shape. The width Δ_{ToF} of the central minimum depends on the excitation time T_{rf} [13]

$$\Delta_{\mathrm{ToF}} = \frac{0.9}{T_{rf}}. \tag{1.16}$$

The magnetic field is crucial for the mass determination, so a reference ion with well-known mass always needs to be measured within a small time frame before and after the ion of interest. Therefore the mass m_x of the atom of interest is expressed as

$$m_x = \left(m_{ref} - m_e\right)\frac{\omega_{c,ref}}{\omega_c} + m_e, \tag{1.17}$$

where ω_c is the ion's cyclotron frequency, $\omega_{c,ref}$ is the reference ion's cyclotron frequency and m_{ref} the mass of the reference ion. Since only singly-charged ions are measured at ISOLTRAP one has to correct for the missing electron mass m_e. At the typical precision level of ISOLTRAP the electron binding energy can be neglected.

ToF-ICR: Ramsey

The Ramsey excitation scheme is just a small modification of the ToF-ICR method. Instead of continuously applying a single RF-pulse for the excitation time T_{rf}, the excitation is applied in two shorter pulses, separated by a certain time interval, adding to the same total measurement time T_{rf} (see Fig. 1.4, right). To achieve the same energy transfer $E_{irr} = \int_0^{T_{rf}} P(t)\mathrm{d}t$ to the ion (and same conversion), the applied power $P(t)$ (amplitude) has to be increased by the same factor by which the actual excitation time has decreased.
The resulting ion-cyclotron resonance plot is shown in Fig. 1.5 (right). The resulting pattern reflects the Fourier transform of the signal envelope, in frequency domain, taking into account that the time-of-flight effect is the lowest for the maximum response in frequency. The advantage of the Ramsey scheme arises from the existence of several minima which constrain the cyclotron frequency, as well as from its narrower central minimum [14]:

$$\Delta_{\mathrm{Ramsey}} = \frac{0.7}{T_{rf}}. \tag{1.18}$$

Since the central minimum is indistinguishable from the other ones, on a narrow frequency range, a ToF-ICR scan has to be performed in advance.

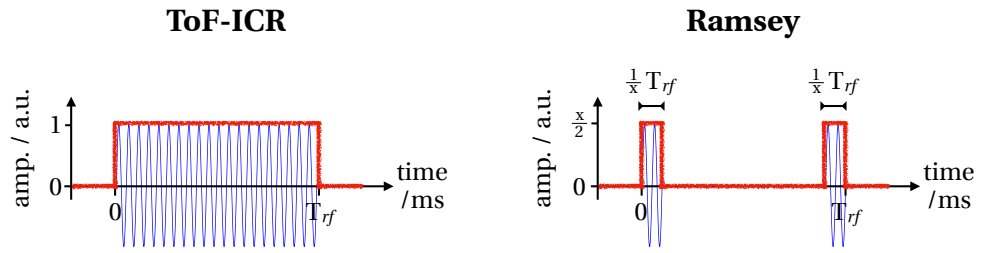

Figure 1.4: Quadrupolar excitation pattern for ToF-ICR in a one pulse (left) and two-pulse or Ramsey-type (right) excitation scheme shown for the same T_{rf}. The red curve shows the signal envelope and the blue line represents the excitation signal in the time domain. The amplitude of the excitation is scaled inverse proportionally to the total length of the excitation pulse, in order to achieve the same effect.

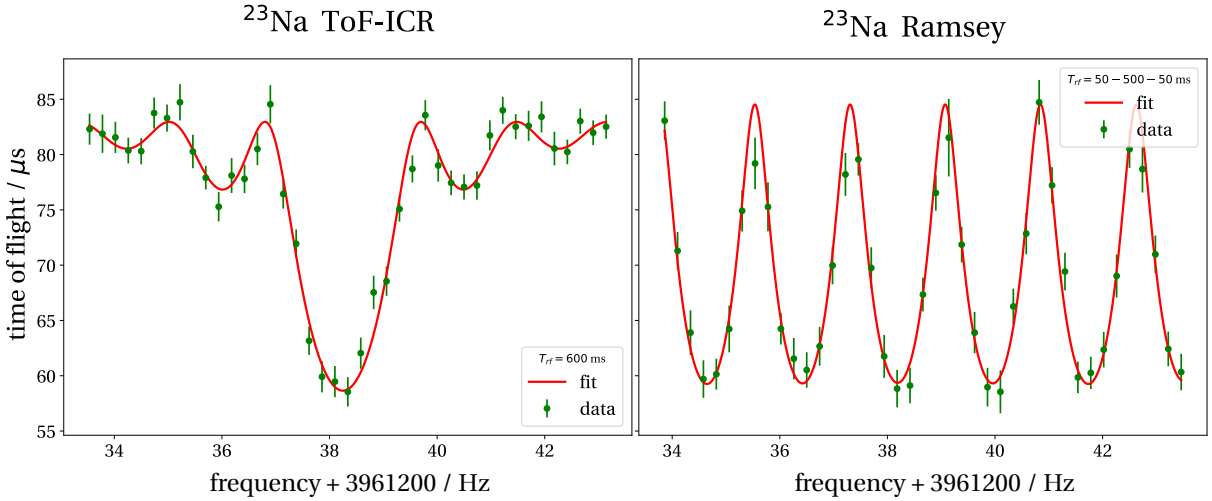

Figure 1.5: Ion-cyclotron resonance with ToF-ICR (left) and Ramsey-ICR (right) shown for ^{23}Na (see also Chapter 3). One notes the difference in width for the central minimum, which is one of the advantages of Ramsey over normal ToF-ICR.

PI-ICR

The destructive PI-ICR method is based on a phase measurement of the radial ion motions. Similar to ToF-ICR the cyclotron frequency is determined by the sum of the magnetron frequency ν_- and the modified cyclotron frequency ν_+. To visualize different states in the trap, the ion motions are magnified by the magnetic field gradient and projected onto a position sensitive detector. The left part of Fig. 1.6 shows a cross section through the upper part of ISOLTRAP's beamline highlighting the precision Penning trap and the position sensitive detector (MCP-PS). The MCP-PS is explained in more detail in Sec. 4.2. The measurement itself takes place in three steps:

- First, a reference spot (also called "C") is taken. Therefore the ions are transported into the precision trap, centered (= reduction of their initial magnetron radius via dipolar excitation at ν_-) and projected onto the MCP-PS. Since they are centered in the Penning trap, they will end up close to the center of the detector. As this position keeps rather constant it is sufficient to measure it with high precision only once a day [12].

- In the next step, excitation pattern one (also called "P1") is applied. Here, the ions are transported to the precision trap, centered then dipole excited at ν_+. This increases the reduced cyclotron radius to a value significantly larger than the size of the ion cloud. Then, the motion is immediately converted with a π-pulse at ν_c to ν_-. At this frequency the ions spend a certain given time t_1 where they accumulate the phase $\phi_- + 2\pi n_-$. Here, n_- represents the number of full turns at ν_-. Right after t_1 the ions are projected onto the detector. The π-pulse frequency ν_c can roughly be determined with a ToF-ICR scan in advance. The corresponding excitation scheme is shown in Fig. 1.7 (left).

- In the final step, excitation pattern two (also called "P2") is applied. The difference to P1 is only in step 4 where the ions are accumulating the phase $\phi_+ + 2\pi n_+$ at ν_+ for a certain given time t_2. n_+ is the number of full turns at ν_+. Here, only after this time the π-pulse is applied and the ions are projected onto the detector. The excitation scheme is shown in Fig. 1.7 (right).

If $t_1 = t_2 := t_{\mathrm{acc}}$ the cyclotron frequency can be calculated by

$$\nu_c = \nu_+ + \nu_- = \frac{2\pi}{t_{\mathrm{acc}}}(n_+ + n_-) + \frac{\phi_{\mathrm{total}}}{t_{\mathrm{acc}}}, \tag{1.19}$$

where $\phi_{\mathrm{total}} = \phi_{\mathrm{P1}} + (2\pi - \phi_{\mathrm{P2}})$ is the total angle between P1 and P2 with respect to the center spot (see Fig. 1.6 (left)). Here, the calculated phase of the P2 spot has to be subtracted from 2π since the P1 and P2 are moving in opposite direction [15].

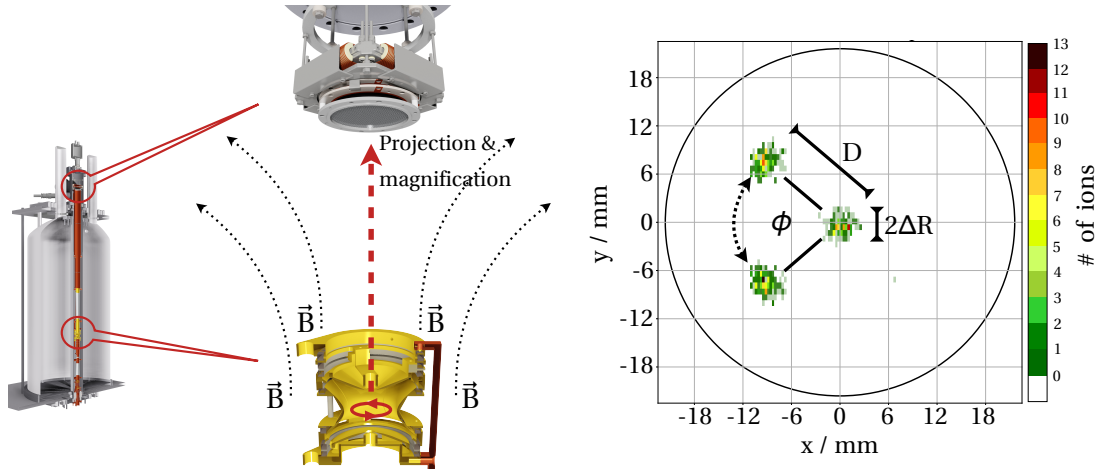

Figure 1.6: PI-ICR principle. The left part shows the projection of an ion's motion inside the Penning trap onto the position sensitive detector MCP-PS (see Sec. 4.2) with details of the upper part of ISOLTRAP's beamline: 5.8 T superconducting magnet (light gray bottle), hyperbolic precision Penning trap (gold), MCP-PS detector and guiding electrodes (copper). The right plot shows a corresponding detector image with the three relevant spots for PI-ICR: the center spot in the middle of the detector and P1 and P2 spots on a circle around the center separated by the angle ϕ. The center and the P1/2 spots are separated by D while their spot size is represented as $2\Delta R$. The spots are taken from real data but are magnified for demonstration purposes. Real measurement data can be found in Sec. 4.4. For details see text.

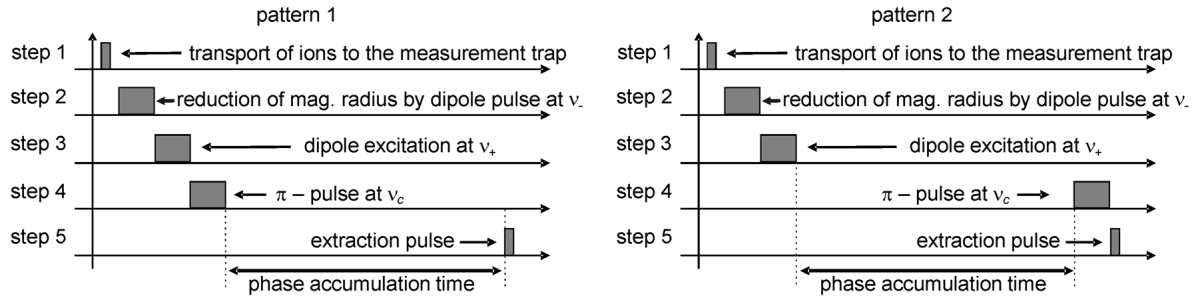

Figure 1.7: PI-ICR excitation schemes. In pattern one the ions accumulate the phase $\phi_- + 2\pi n_-$ at ν_- and in pattern two the phase $\phi_+ + 2\pi n_+$ at ν_+. [12]

1.2 MR-ToF MS

A Multi-Reflection Time-of-Flight (MR-ToF) device is an ion trap which consists of a pair of electrostatic mirrors. It keeps charged particles of an initial kinetic energy E_0 on a stable path between the mirrors. Due to different velocities of ions with same E_0 but different mass the device can be used for beam purification or mass determination.

The principle is shown in Fig. 1.8 where both mirrors consist of 6 electrodes. The beam enters to the right with a kinetic energy higher than the first mirror potential and enters the cavity (dark grey area). By switching the voltage of the in-trap lift electrode [16] the total beam energy of the ions within the cavity is reduced such that the ion's kinetic energy becomes lower than the mirror potentials. Therefore the ions will be trapped and oscillate between the two mirrors. Thanks to the specific potential even ions with slightly different energy or trajectory than the average ion will have the same flight path (= time focus). A typical trapping at ISOLTRAP is on the order of 1000 revolutions inside the MR-ToF leading to a flight path > 1 km. Since all ions enter the trap with the same energy, the ones with a smaller/larger mass will separate and end up having a larger/smaller time of flight leading to a mass resolving power $R > 10^5$ at trapping times $t_{trapping} < 10$ ms (see also Fig. 1.9). The separated ions are ejected the same way as they were trapped, via fast cavity switching [16]. It is also possible to apply a higher mirror potential than the beam energy and switch the entrance and exit mirrors instead. This however requires very stable and very fast switching HV-power supplies but allows on the other hand filling the trap for more than twice time available when using cavity switching.

The abbreviation MS in MR-ToF MS stands for Mass Separator or Mass Spectrometer. The first application can be achieved by switching forth and back the cavity for ejection when the ion of interest is separated and about to be reflected at the exit mirror so that only this bunch would leave the device. At ISOLTRAP this is used for isotope separation as preparation for Penning-trap mass spectrometry. The second mentioned application is used by precisely measuring the ToF of ions starting at the moment when they enter the device and ending when they reach a detector (typically an electron multiplier) behind the device. In practice,

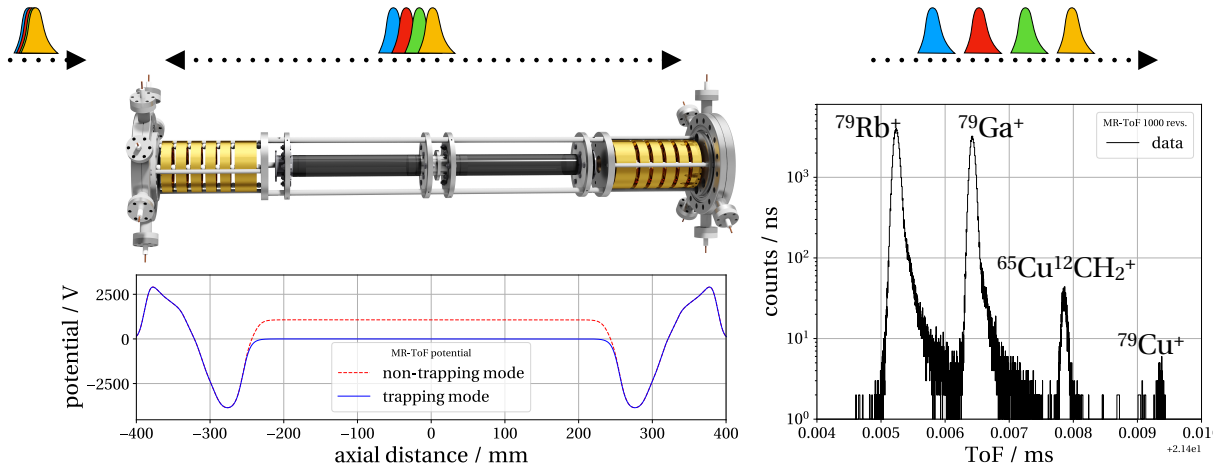

Figure 1.8: Schematic overview of an MR-ToF device. On top the principle of mass separation is shown, below on the left side is a rendering of the ISOLTRAP MR-ToF MS where the mirror electrodes are displayed in gold and the cavity in dark gray. Below the rendering the axial potential for trapping mode and non-trapping mode (= injection/ejection of ions) is plotted. [17] The right plot shows a mass measurement for ^{79}Cu with a huge contamination but successful separation after 1000 revolutions. The counts in ns-binning are plotted against the ToF of the ions. [18]

the moment when the ions are ejected towards the MR-ToF MS from the cooler and buncher in front of it is taken as time origin. The big advantage in both cases is the capability of separating the ion of interest even with high contamination rates $R_{cont.} \gg 1000$ (see right plot in Fig. 1.8 for ^{79}Cu). For further details the reader is referred to the literature [17, 19–21]

Penning trap vs MR-ToF-MS

A good comparison quantity between different devices in mass spectrometry is the mass resolving power R. In ToF-ICR, minimal separation is achieved when two resonance centroids are separated by two FWHM of the resonance minimum. Therefore, the mass resolving power in ToF-ICR depends on the width of the central minimum (see Fig. 1.5) and the centroid frequency:

$$R_{\text{ToF-ICR}} = \frac{\nu}{2 \cdot \text{FWHM}_\nu} . \tag{1.20}$$

In PI-ICR, minimal separation is achieved when two spots on the position sensitive detector are separated by two FWHM of the spot size. It hence depends on the angular peak width ϕ_{spot}, see Fig. 1.6 and Eq. (4.1)) and the full phase of the motion:

$$R_{\text{PI-ICR}} = \frac{\phi_{\text{total}}}{2 \cdot \phi_{\text{spot}}} . \tag{1.21}$$

For MR-ToF MS, minimal separation is achieved when two ToF peaks are separated by two FWHM. The mass resolving power thus depends on the width of the ToF peak (see Fig. 1.8) and its time of flight:

$$R_{\text{MR-ToF MS}} = \frac{\text{ToF}}{2 \cdot \text{FWHM}_{\text{ToF}}} . \tag{1.22}$$

Figure 1.9 shows the mass resolving power R of a Penning trap in comparison with an MR-ToF MS for a singly charged ion with $A = 100$. From it one can deduce that the Penning trap is superior for large measurement times. Therefore one favors it for high-precision mass spectrometry. On the other hand the MR-ToF has advantages for very short measurement times < 100 ms, which are needed for mass spectrometry on short lived isotopes especially considering its ability to handle high contaminations. But even in short-lived cases the newly installed PI-ICR method outperforms the MR-ToF MS.

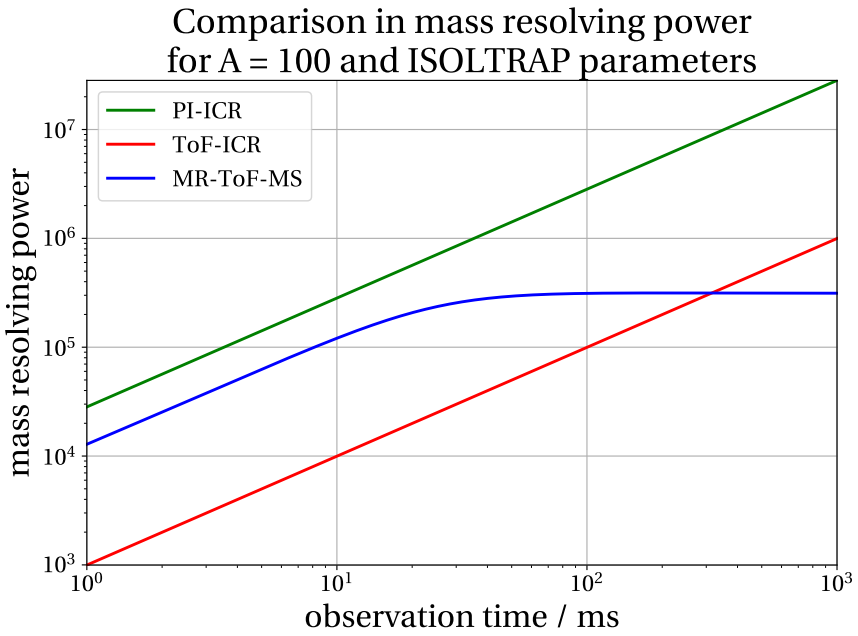

Figure 1.9: Comparison in mass resolving power R for a singly charged ion for MR-ToF-MS[17] (blue), ToF-ICR (red) and PI-ICR (blue) shown for $A = 100$ and parameters fitting to the current situation at ISOLTRAP. Figure courtesy of Frank Wienholtz.

2 The ISOLDE facility and the ISOLTRAP experiment at CERN

This chapter introduces the mass spectrometer ISOLTRAP, which is situated at the radioisotope facility ISOLDE at the European Organization for Nuclear Research (CERN). The ion production and separation process at ISOLDE is discussed and the experimental setup of ISOLTRAP is illustrated in detail in the context of mass spectrometry.

2.1 CERN

The European Organization for Nuclear Research (CERN, *French: Conseille Européen pour la Recherche Nucléaire*) is a major research institution close to Geneva, Switzerland, highlighted in Fig. 2.1 and Fig. 2.2. It is the world's largest Particle Physics laboratory having as its core the Large Hardron Collider (LHC) being the world's largest and most powerful particle accelerator and collider.

Figure 2.1: Map of Europe with Geneva highlighted in red. [22]

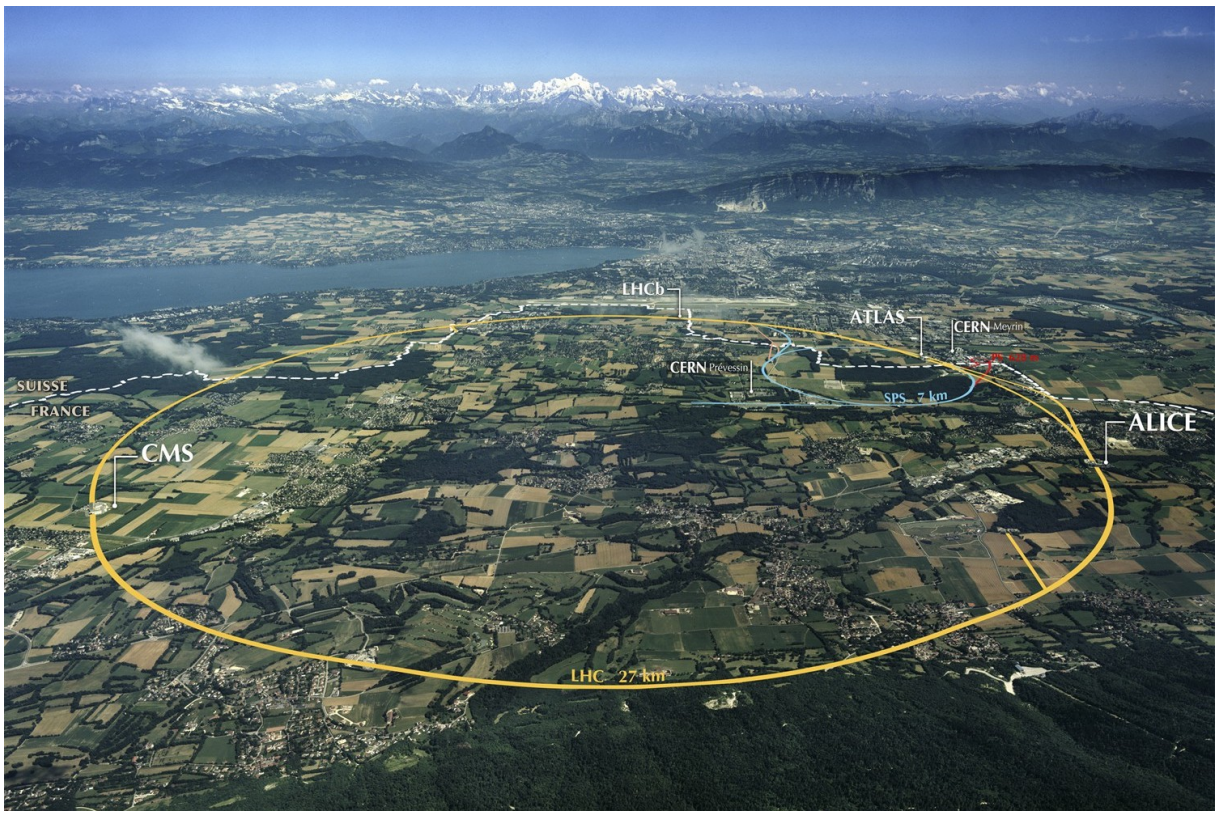

Figure 2.2: Bird's eye view of CERN. The photo was taken over the Jura towards south-east. The lower part shows the French territory between the Jura (down) and Lake Geneva (middle-left) whereas the upper part shows Geneva, Switzerland (in the middle at the end of Lake Geneva), and the Alps dominated by Mont Blanc. CERN facilities and accelerators are shown schematically. Photo[23] cut to a 3:2 aspect ratio.

CERN constists of a sequence of different accelerators but everything starts with a small bottle of H_2. First the electrons are stripped off to get free protons. In the next step the protons are accelerated in the Linear Accelerator (Linac2, length = 30 m, E_{p+} = 50 MeV), leading to the Proton Synchrotron Booster (PSB, circumference = 157 m, E_{p+} = 1.4 GeV), the Proton Synchrotron (PS, circumference = 628 m, E_{p+} = 28.3 GeV), the Super Proton Synchrotron (SPS, circumference = 6912 m, E_{p+} = 450 GeV) and the Large Hardron Collider (LHC, circumference = 26659 m, E_{p+} = 7.5 TeV). Here E_{p+} is the typical proton exit energy or maximum proton energy for the LHC. At each transfer point between two accelerators it is also possible to guide the protons to different facilities specialized for that proton energy. The ISOLDE (see Sec. 2.2) facility for example is situated right behind the PSB. At CERN it is also possible to accelerate heavy ions like lead ions or to produce antimatter.

2.2 ISOLDE

The Isotope Separator On Line DEvice (ISOLDE) [24–26] is a facility at CERN for the production of radioactive ion beams. It was build in 1967 as one of the first experiments at CERN and was moved in 1992 to the PSB accelerator at CERN. There it impinches 1.4 GeV accelerated protons on a thick target to produce a vast variety of radioactive nuclides of 75 different chemical elements [26] and delivers them to many different experiments [27]. ISOLDE was the first Isotope-Separation-On-Line (ISOL) facility and made during its over 50 years of existence major contributions to physics topics such as nuclear physics, nuclear astrophysics, solid state physics and even fundamental interactions, with emerging fields such as radioisotope research for biophysics and medicine. A detailed summary of the research activities at ISOLDE can be found in the ISOLDE Laboratory Portrait, which was published as a collection of articles in a special volume of Journal of Physics G [28].

2.2.1 Overview

In Fig. 2.3 a schematic overview of the ISOLDE facility is shown. The PSB proton beam arrives on the right-hand side at an energy of 1.4 GeV and an intensity up to 2 μA [25]. There it hits one of the two target stations and produces many different kinds of isotopes (for more information read Sec. 2.2.2). After ionization the beam is re-accelerated to 30-60 keV, magnetically separated and guided towards the different experiments.

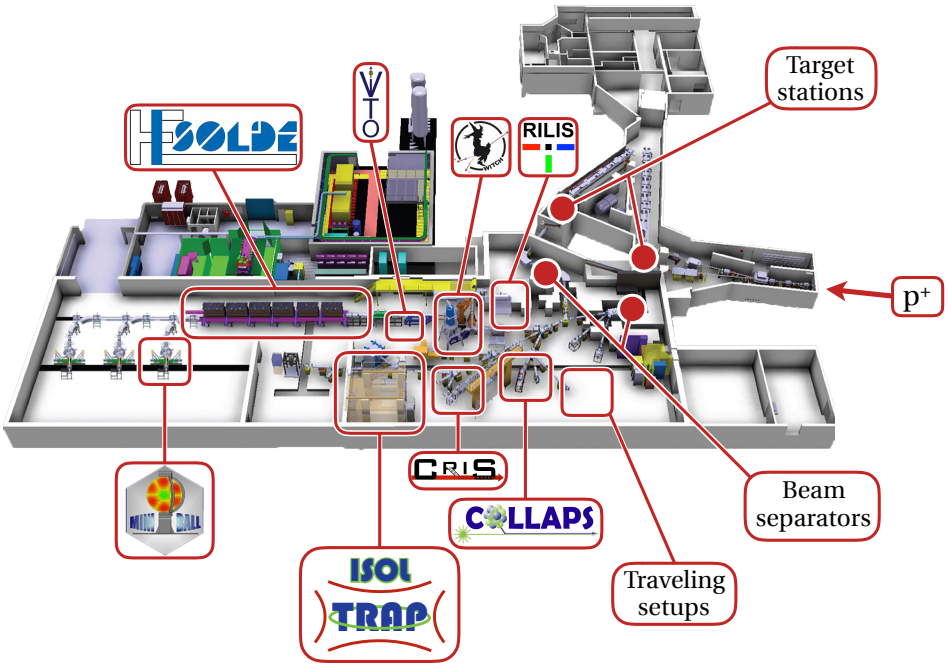

Figure 2.3: Overview of the ISOLDE facility at CERN. The 1.4 GeV proton beam from the PSB enters on the right-hand side and hits one of the two target stations. After ionization the beam is separated by one of the two magnetic separators and guided towards the experiments. Shown is a selection of local experimental setups in alphabetical order: CRIS, COLLAPS, HIE-ISOLDE, ISOLTRAP, MINIBALL, RILIS, VITO, WITCH.

2.2.2 Ion production

The method of isotope production at ISOLDE is to induce nuclear reactions on a target consisting of very heavy atoms bound in a crystalline structure or a liquid (e.g. uranium-carbide UC_x or molten lead, respectively). The PSB proton beam is either shot directly onto the target material or onto a neutron converter placed right next to the target material, which allows bombarding the target with fast neutrons instead of protons. This increases the production of neutron-rich isotopes. Due to nuclear fission, spallation or fragmentation the heavy target nuclei are broken down into many lighter radionuclides (see Fig. 2.4).

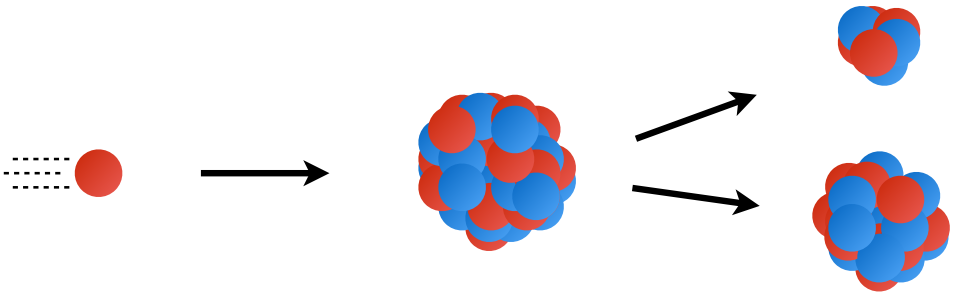

Figure 2.4: Schematic spallation process. Protons are shown in red, neutrons in blue. A fast proton hits a heavy target nucleus and breaks it into two smaller nuclei while conserving the barion number.

To ensure an efficient and fast diffusion of the produced nuclides the target is heated resistively to up to 2000°C or even more [26]. Figure 2.5 shows the yield of ions which are produced with a typical UC_x target at ISOLDE. After production the initially neutral atoms still have to be ionized in order to accelerate and guide them to the experiments. Three options are available at ISOLDE for ionization:

1. A surface ion source is the simplest such method, for which atoms pass through a thin metallic tube heated to high temperatures (< 2400°C) and stick to its surface. The surface material has a higher work function than the atom to be ionized which favors the release of an electron by the atom, thus forming single ions.

2. A plasma ion source is used to ionize atoms that do not undergo efficient surface ionization. In this case the atoms pass a plasma of a gas mix (e.g. Ar+Xe) which was preionized by electron bombarding. To stabilize the plasma an additional magnetic field has to be applied.

3. A very elegant way of ionizing atoms is via laser excitation performed by RILIS at ISOLDE [29]. The advantage of this method is that only the element or in some cases even isotope or isomer of interest is ionized due to their specific excitation schemes and isotope shifts.

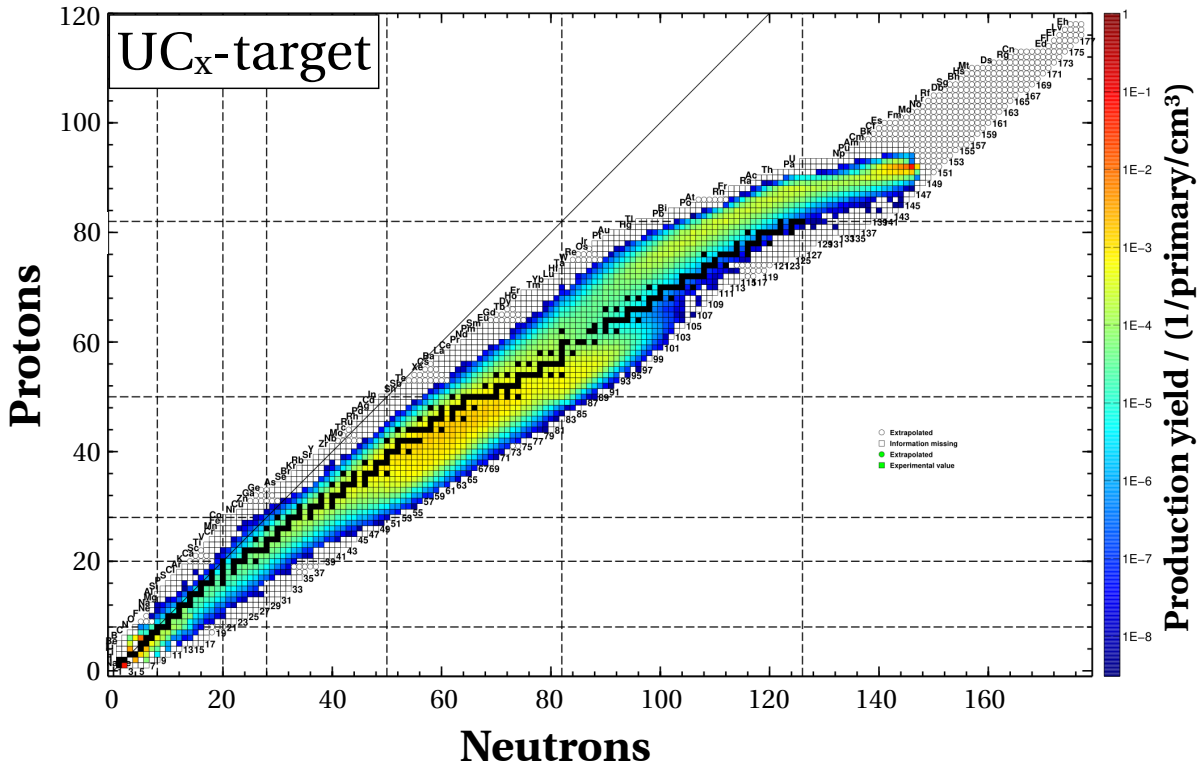

Figure 2.5: Nuclear chart with yield information at ISOLDE for a UC_x target and irradiation by 1.4 GeV protons. For particular areas of the nuclear chart other target materials might produce larger yields. Figure courtesy of Frank Wienholtz.

2.2.3 Separation

Before reaching the experiments the ion beam is mass separated by dipole magnets. The separation is achieved by the fact that the Lorentz force in a magnetic field $\vec{F}_{L(mag)} = q\vec{v} \times \vec{B}$, where the velocity is mass dependent, deflects ions of different mass by different amounts. The General Purpose Separator (GPS) consists of one bending magnet and reaches a mass resolving power of $\frac{m}{\Delta m} \approx 800$ whereas the High Resolution Separator (HRS) consists of two bending magnets and reaches a mass resolving power of $\frac{m}{\Delta m} \approx 6000$ [25].

2.3 ISOLTRAP

ISOLTRAP is a permanent mass spectrometer at ISOLDE/CERN which was installed already in 1987 and was constantly improved and upgraded. The experiment is mainly dedicated to precision mass measurements of short-lived isotopes with half-lives down to the millisecond regime [19, 30, 31].

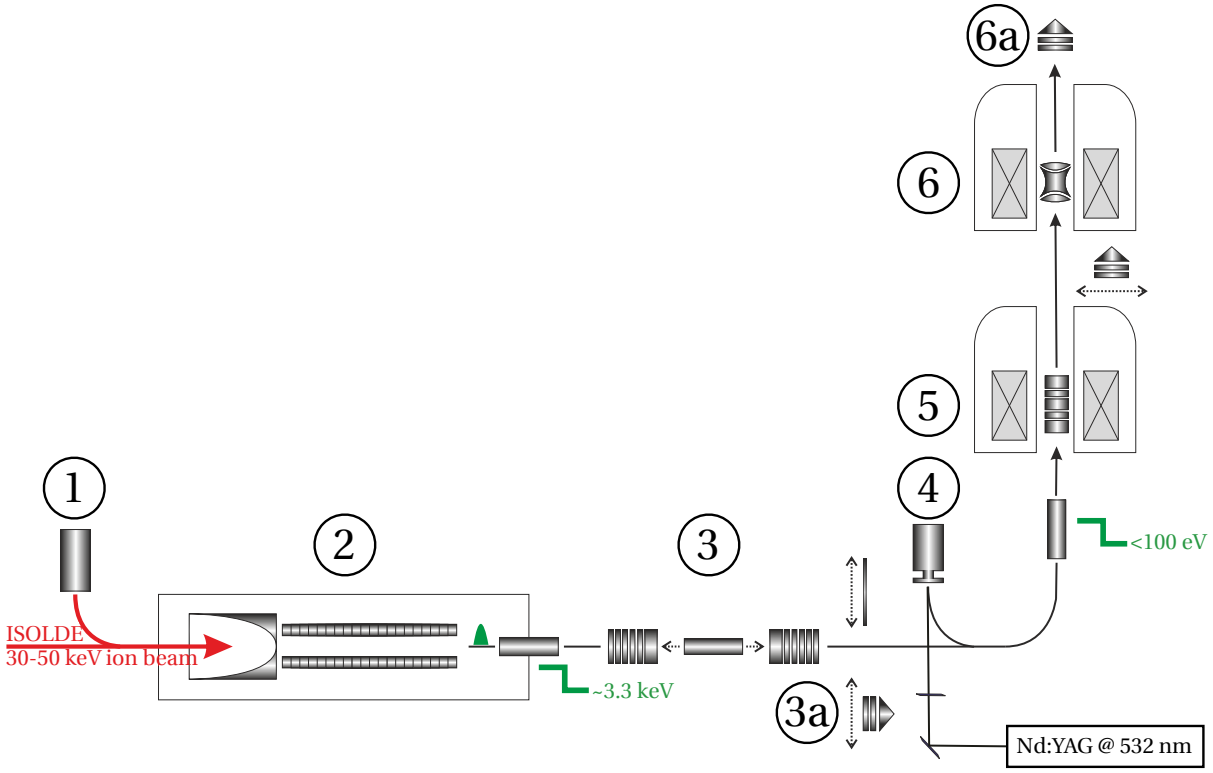

Figure 2.6: Schematic overview over ISOLTRAP. 1 = alkali ions source, 2 = radio-frequency quadrupole (RFQ) cooler and buncher, 3 = multi-reflection time-of-flight mass separator and spectrometer (MR-ToF MS), 3a = electron multiplier (EMP2H), 4 = laser ion source, 5 = preparation Penning trap, 6 = precision Penning trap, 6a = position sensitive detector (MCP-PS). Ions from ISOLDE enter to the left at an energy of 30-50 keV. Towards the precision trap the beam energy is reduced in several steps by cavity switching to a few tens of eV.

The setup which is shown in Fig. 2.6 spans over ~ 4 m in the horizontal plane and ~ 7 m in the vertical plane. The ion beam provided by ISOLDE enters to the left at possible energies of 30-50 keV. In addition one can use an alkali offline-source (**1**) to tune the setup and as reference for the $\vec{B}$-field calibration (see Sec. 1.1.3). Usually one uses $^{133}Cs^{+}$, $^{85,87}Rb^{+}$ and $^{39}K^{+}$ for these purposes. All ions first reach the Radio-Frequency Quadrupole (RFQ, **2**) which cools and bunches the beam with He-gas in ~5-100 ms [32–34]. Then the bunch exits the RFQ and enters a pulsed drift tube, biased to about 3.3 kV lower voltage than the RFQ. When the ions are inside the tube, its voltage is switched to ground, preventing the re-acceleration of the ions to more than 3.3 kV. Subsequently, the ions enter the MR-ToF MS [17, 19, 21](**3**) where they are further separated by mass ($R = \frac{m}{\Delta m} \approx 10^5$ at ~30 ms for $^{133}Cs^{+}$ corresponding to 1000 revolutions [19]). For very short-lived isotopes it can also serve as a mass spectrometer (see

Fig. 1.8) by using an electron multiplier (**3a**). At this stage (**4**) there are optional ports for a laser ablation ion source [9]. In the next step the ions are bent upwards by 90°. The beam energy is further reduced by cavity switching to < 100 eV and the ions reach the preparation Penning trap [35] (**5**). It is a cylindrical Penning trap inside a 4.7 T superconducting magnet which is filled with helium buffer gas. The trap's ring electrode is 8-fold segmented allowing dipolar, quadrupolar or even higher excitation schemes [36]. This Penning trap is used to further cool the beam and clean it from isobaric contaminations ($R_{typical} \approx 10^5$, sufficient to remove most of the isobaric contaminants) [32]. Finally the ions reach the hyperbolic precision Penning trap (**6**, see also Fig. 1.6) placed in a 5.9 T superconducting magnet, where the mass can be determined via the ToF-ICR [37] or PI-ICR [1, 2, 12] detection techniques (see Sec. 1.1.3). For both methods a position sensitive multi-channel plate detector in Chevron layout (MCP-PS, **6a**, see Sec. 4.2) is used in order to determine the ToF and/or to image the ions' motion inside the trap.

3 High-precision Q-value measurements with the Ramsey-ToF-ICR detection technique

This chapter introduces the latest results of high-precision Q-value measurements of the β-decay pairs ^{21}Na/Ne and ^{23}Mg/Na at ISOLTRAP. First the concepts of Q-value and mirror nuclei are introduced while emphasizing their relevance for weak interaction studies, specifically tests of the Conserved Vector Current (CVC) hypothesis and determination of the V_{ud} element of the Cabibbo– Kobayashi–Maskawa (CKM) quark-mixing matrix. Second the measurement itself as part of the IS565 experiment is explained. Finally the analysis of the data set is presented in detail.

3.1 Q-value of mirror-nuclei decays

The presented data results from a beam time [38], which was performed with a set of nuclides called "mirror nuclei". They represent a special case of isobars (= isotopes with the same mass number) by the fact that they are obtained from each other by interchanging the number of protons and neutrons. In the Bethe-Weizsäcker-equation [39, 40] the binding energy of mirror nuclei simply differentiates by the Coulomb part due to the different number of protons.

Q-value concept

The Q-value is calculated as the difference between the atomic mass of the mother and daughter nuclide times the speed of light:

$$Q_\beta = (m_{mother} - m_{daughter}) \cdot c^2 \,. \tag{3.1}$$

If one determines by Penning-trap mass spectrometry the frequency ratio between singly-charged ions of the two species, $R_\nu = \frac{\nu_{c,daughter}}{\nu_{c,mother}}$, then one can use it to determine the Q-value as:

$$Q_\beta = (R_\omega - 1) \cdot \left(m_{daughter} - m_e\right) \cdot c^2 \,, \tag{3.2}$$

where m_i with $i \in [mother, daughter, e]$ is the mass of the mother isotope, the daughter isotope and the emitted electron or positron, respectively.

Physics case

In this special case a precise determination of the Q-value can provide, together with other quantities, one of the best tests of the Conserved Vector Current (CVC) hypothesis, and the most precise determination of the V_{ud} element of the Cabibbo–Kobayashi–Maskawa (CKM) quark-mixing matrix.

The quantity of interest is the so-called corrected $\mathscr{F}t$-value. It derives from the ft-value which is nearly independent of nuclear-structure ambiguities (~1%) [41]. The experimental ft-value derives from three measured quantities: the transition energy of the β-decay, the half-life $T_{1/2}$ and the branching ratio R. Since the measurement parameters include also the small nuclear-structure corrections, it is convenient to define a corrected $\mathscr{F}t$-value, which for pure Fermi transitions only depends on the vector part of the weak interaction:

$$\mathscr{F}t := ft \cdot (1+\delta'_R) \cdot (1+\delta_{NS}-\delta_C) = \frac{K}{2G_V^2 \cdot (1+\Delta_R^V)} \,. \tag{3.3}$$

Here, $\frac{K}{(\hbar c)^6} = \frac{2\pi^3 \hbar \ln 2}{(m_e c^2)^5} = 8120.271(12) \cdot 10^{-10} \frac{\mathrm{s}}{\mathrm{GeV}}$, G_V is the vector coupling constant and Δ_R^V is the transition-independent part of the radiative correction. Furthermore, δ'_R and δ_{NS} combined represent the transition-dependent part of the radiative correction and δ_C is the isospin-symmetry-breaking correction [41]. Therefore, by determining the $\mathscr{F}t$-value one can verify whether G_V is an universal constant (CVC hypothesis), or whether it is renormalized in the environment [42].

The CKM quark-mixing matrix is a unitary 3x3 matrix. It describes the correlation between the quark-flavor content of an initial state and a final state after interaction with a flavor-changing particle (e.g. W-boson). It is defined as

$$V_{\mathrm{CKM}} = \begin{pmatrix} V_{ud} & V_{us} & V_{ub} \\ V_{cd} & V_{cs} & V_{cb} \\ V_{td} & V_{ts} & V_{tb} \end{pmatrix} \tag{3.4}$$

$$= \begin{pmatrix} 0.97434 \pm 0.00021 & 0.2248 \pm 0.0006 & 0.00409 \pm 0.00039 \\ 0.220 \pm 0.005 & 0.995 \pm 0.016 & 0.0405 \pm 0.0015 \\ 0.0082 \pm 0.0006 & 0.0400 \pm 0.0027 & 1.009 \pm 0.031 \end{pmatrix} \tag{3.5}$$

with the elements V_{ij}, the initial flavor i and the final flavor j. Here, $i, j \in [u, d, t, b, c, s]$ with the flavors u = up, d = down, t = top, b = bottom, c = charm and s = strange. The measured matrix-element values are taken from [43] where in Ch. 12 one can also find detailed information about the matrix and its properties. The unitarity can be tested by the condition that

the sum of the squares of the elements in a row/column of the matrix is 1. Taking selected values from [43], one obtains

$$|V_{ud}|^2+|V_{us}|^2+|V_{ub}|^2 = 0.9996 \pm 0.0005 \quad \text{(1st row)} \tag{3.6}$$

$$|V_{cd}|^2+|V_{cs}|^2+|V_{cb}|^2 = \quad 1.040 \pm \quad 0.032 \quad \text{(2nd row)} \tag{3.7}$$

$$|V_{ud}|^2+|V_{cd}|^2+|V_{td}|^2 = 0.9975 \pm 0.0022 \quad \text{(1st column)}\,. \tag{3.8}$$

The first row is the most precisely determined yet of all possible combinations. Here, the V_{ud}-element plays the dominant role in the sums as it has the largest value. The most precise determination of $V_{ud} = G_V/G_F$ comes from the study of super-allowed $0^+ \rightarrow 0^+$ transitions [43], where the vector-coupling constant G_V can be derived from the $\mathcal{F}t$-value. The weak-interaction-coupling constant G_F can be determined from purely leptonic muon decay studies.

In the case of this work, the measurements addressed a new class of decays, namely $T = 1/2$ decays between mirror nuclei [38]. These decays are of mixed Fermi/Gamow-Teller type and depend both on the vector and axial-vector part of the weak interaction. The only complication with respect to the pure Fermi decays is that the left-hand side of Eq. (3.3) contains an additional multiplicative term $\left(1+\frac{f_A}{f_V}\rho\right)$, where f_A and f_V are the statistical rate functions for the axial-vector and vector parts of the interaction, respectively, and ρ is the Fermi/Gamow-Teller mixing coefficient. This coefficient must be also determined experimentally, before a reliable extraction of V_{ud} is possible. More information can be found in [44].

3.2 Mirror-nuclei measurement and data analysis

In the following the analysis of a data set resulting from an ISOLTRAP beam time from 2016, part of the IS565 [38] experiment will be presented. The run took place on GPS with a SiC target and a hot plasma ion source (see also Sec. 2).

Beam time information

The run aimed at a high-precision ($\sim 20\,\text{eV}$) determination of the β_+ decay Q-value between the isobars ^{21}Na/Ne and ^{23}Mg/Na. No offline reference ions from ISOLTRAP are necessary in those cases since one can alternatively measure the cyclotron frequencies of the mother and daughter nuclei directly from ISOLDE. Reference measurements were however performed to monitor the stability of the setup. The difference in mass between the mother and daughter nuclei are big enough for them to be resolved in the MR-ToF MS. This allowed already a separation of the isotopes before their transfer to the Penning traps. To reduce systematic uncertainties and to minimize temperature-dependent B-field drifts the measurement was performed alternating between the mother and daughter nuclei in $\sim 20\,\text{min}$ intervals.

Furthermore the measurement was periodically changing between the different masses as well as reference ion measurements (^{39,41}K from ISOLTRAP's offline source) which allowed to check the system's stability.

Analysis

The measured ToF-spectra were fitted with the analysis software EVA [45]. To cross-check, random spectra were additionally analyzed with a custom ROOT [46, 47] analysis software using an independent algorithm. The analysis was performed as usual independently by two physicists and is in well agreement. Figure 3.1 summarizes the determined masses of ^{21}Na and ^{23}Mg from all measurements of IS565 beamtime using ^{21}Ne and ^{23}Na as reference ions. The green points indicate Ramsey measurements and the red ones TOF-ICR check measurements, well agreeing within their uncertainty.

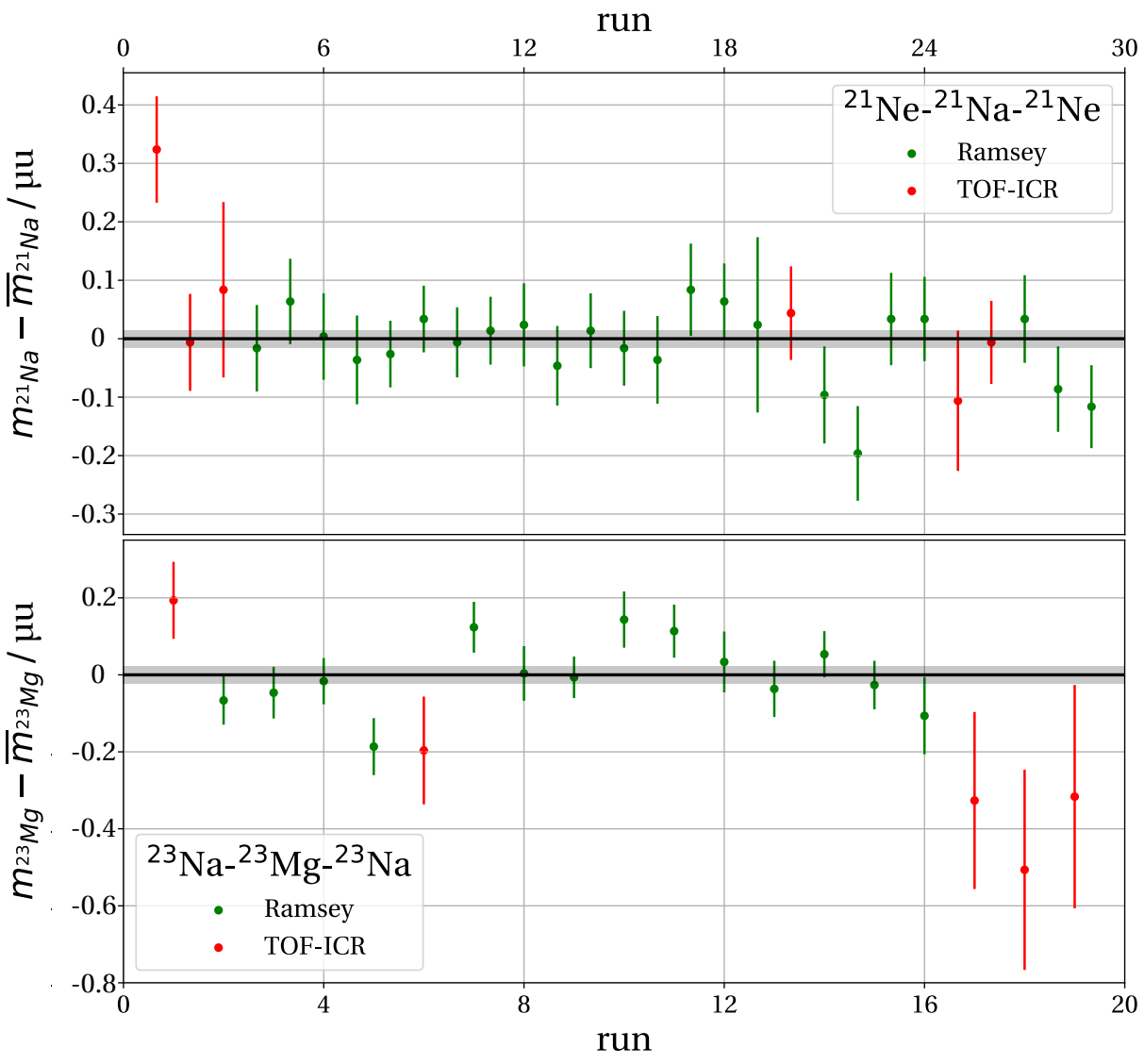

Figure 3.1: Masses of ^{21}Na and ^{23}Mg from all measurements of the IS565 beamtime, using ^{21}Ne and ^{23}Na as reference ions, respectively.

The analysis followed the one described in [45]. The statistical uncertainty of each time-of-flight value in the resonance was set as $\frac{\sigma}{\sqrt{N}}$ where σ is the standard deviation of the time-of-flight distributions and N is the number of measured ions. Hereby, for all files a single value of σ was used which was calculated in advance as an average over all frequency channels in the resonance. The statistical uncertainty was then augmented by quadratically adding the systematic uncertainty quantifying the non-linear magnetic field drifts. Finally all frequency ratios were computed using weighted averaging [48]. Since the mother and daughter ions were isobaric in all cases and the measurements were performed with identical conditions, no further systematic uncertainties were considered.

Result

In the measurement a final precision of $2.1 \cdot 10^{-9}$ ($\chi^2_{\mathrm{red}} = 1.03$) for ^{21}Na and $1.3 \cdot 10^{-9}$ ($\chi^2_{\mathrm{red}} = 1.07$) for ^{23}Mg was reached. The final Q-values are summarized in Tab. 3.1. A significant reduction of the Q-value uncertainty for both studied cases was achieved using the Ramsey excitation scheme in ToF-ICR. The offline cross-checks show in terms of scattering and drifts that the setup seemed to have been stable during the whole beam time. These results will be published soon.

Table 3.1: Q-value results of the β-decay pairs ^{21}Na/Ne and ^{23}Mg/Na in comparison to AME16 [49].

	β⁺-decay	**Q-value / keV**	**unc. / keV**
ISOLTRAP	^{21}Na→^{21}Ne	3546.890	0.019
AME16		3547.145	0.105
ISOLTRAP	^{23}Mg→^{23}Na	4056.176	0.032
AME16		4056.339	0.158

4 Improvement and characterization of the PI-ICR detection technique at ISOLTRAP

The previous chapter introduced the latest results of the commonly-used ToF-ICR mass spectrometry method, showing the current state of the art in the field of mass-spectrometry of radioactive isotopes (with stable isotopes higher precision can still be achieved by longer excitations times or by using the FT-ICR detection technique). However the requirement of measuring ions with even shorter life times or with ultra-low production yields challenges the current standard in Penning-trap mass spectrometry. The newly developed PI-ICR [1, 2] method is a promising approach for pushing even further the boundaries of what can be measured with a Penning trap. After its implementation at ISOLTRAP in 2016, this work was aimed at improving and characterizing a number of systematic problems. To adapt the drift region in the magnetic field gradient to the requirements of the PI-ICR detection technique, a simulation of the guiding voltages was performed, which pointed to the necessity of lowering the detector towards the precision Penning trap. Furthermore, a position reconstruction and analysis software were written in the context of this thesis in Python. Finally a systematic online study of the ^{88}Rb-^{88}Sr β-decay Q-value pair was performed and analyzed as a validation of the PI-ICR detection technique at ISOLTRAP.

4.1 Simulation and studies

Initial situation

Figure 4.1 shows the layout of the beam line leading into the precision Penning trap and up to the position-sensitive detector in October 2016. The precision Penning trap is preceded by a long transfer section connecting it to the preparation trap, which ends with a lens, a steerer and a pair of deceleration drift tubes. The lens called UT3 is responsible for the final focusing of the ions into the trap, while the steerers called UT2x/y are used to adjust the injection angle, in order to achieve a minimum initial magnetron radius. Finally, the two retardation electrodes called Retardation 1 and 2 ensure a two-step deceleration of the ion beam from the 1 keV transport energy to zero. The transport of the ions from the trap to the detector is achieved by a set of drift tubes (seven in total) and the final focusing on the

detector is obtained using an einzel lens. As one can see there are several focusing electrodes to optimize the ~ 1.2 m long path. Simply setting a constant voltage on all of them is not possible due to the defocusing effect of the magnetic-field gradient. In the original setup the detector is placed in a 6-way cross, which breaks the cylindrical symmetry of the potential distribution and can lead to distortions.

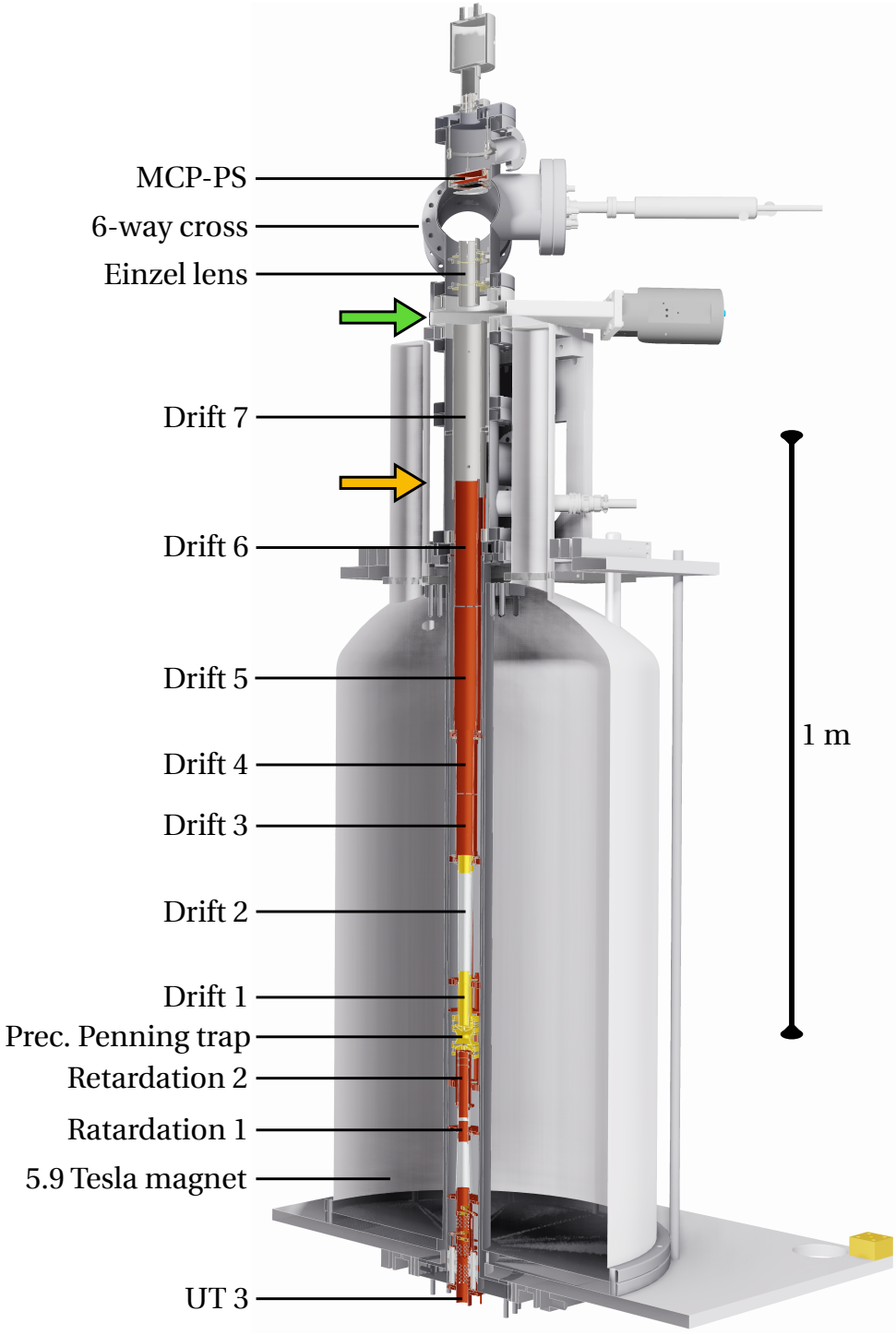

Figure 4.1: Drawing of the ISOLTRAP upper beam line surrounding the precision trap in 2016. Shown is the precision Penning trap in the 5.9 T superconducting magnet, several drift tubes, an einzel lens, a 6-way-cross, the position sensitive detector and a 1 m scale. The two colored arrows indicate alternative detector positions (for details, see text).

During the first on-line and off-line tests of the new PI-ICR detection technique performed in the first half of 2016 [50], five major problems were identified:

1. The spot size on the position sensitive detector (= MCP-PS) was consistently larger than 3 mm FWHM and often larger than 5-6 mm.

2. The spot shape was in general not spheric.

3. The center spot showed a deviation from the center of the detector which reduced the usable area on the detector.

4. The spot distribution on the 2π phase clock (= plot with 6 P1-spots, each with an additional phase $\phi_{\text{add}} = 2\pi n_{\text{add}}$ with $\frac{n_{\text{add}}}{n_{\text{P1}}} \in [\frac{1}{6}, \frac{2}{6}, \frac{3}{6}, \frac{4}{6}, \frac{5}{6}, \frac{6}{6}]$ and n_{P1} one full round on P1; also see Fig. 4.7) was not circular, but ellipsoidal or otherwise distorted.

5. A fast detector saturation (for as little as 2 events per cycle) was observed.

To solve the first four problems listed above, the initial general strategy was to perform manual voltage optimization. However, this approach rarely allowed optimizing both the spot size, phase-clock symmetry and general ratio of spot size to spot distance to the center (= resolving power). Moreover the optimal settings weren't stable over time. To illustrate this problem, below are presented some typical scans of ion transport voltages, as they are reflected in the spot size and distance from the center of the detector.

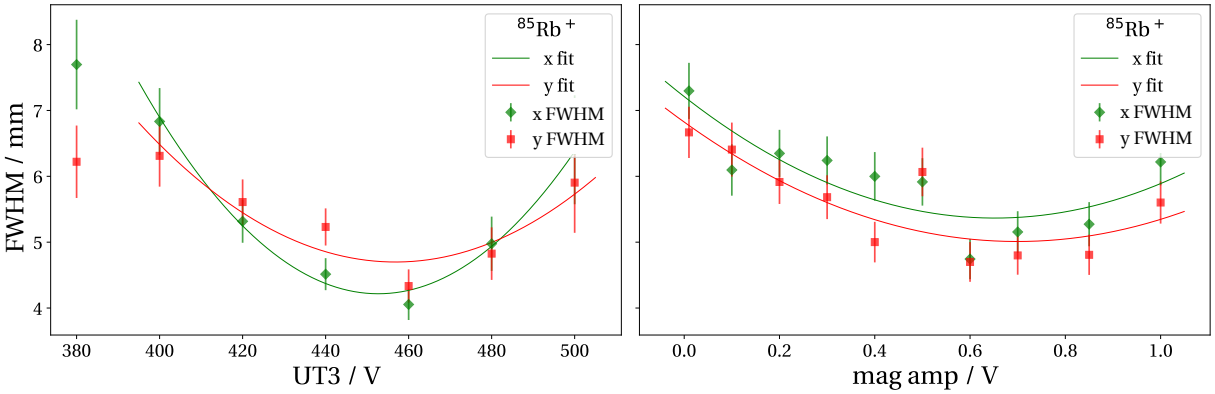

Figure 4.2: Scans of the voltage of the last lens before the precision trap (UT3) and of the amplitude of the magnetron excitation (used to reduce the initial magnetron radius). The FWHM of the ion spot in both X and Y are represented.

Figure 4.2 shows the variation of the size of the ^{85}Rb spot with the voltage of the last lens before the precision trap (UT3) and of the amplitude of the magnetron excitation. The latter is used to reduce the initial magnetron radius. The FWHM of the ion spot in both X and Y are represented. Even a small change in voltage leads to a significant change in spot size, while the optimal value is still above 4 mm. This makes manual optimization very time consuming, with so many free parameters. To obtain the voltage of minimal FWHM, a polynomial fit was used for each data set.

Another issue can be illustrated by varying the voltage of the middle einzel lens electrode as shown in Fig. 4.3. The spot size but also the spot position seem to be strongly dependent on the voltage of the focusing electrode, so the einzel lens potential also induces a steering. This can only be explained by a misalignment of the upper section of the beam line since a similar steering effect doesn't seem to appear so much for the drift tubes. During the initial tests, this observation indicated that the upper 6-way cross in which the detector was placed and which was separated by a bellow from the rest of the trap extraction optics could be the source of the misalignment. Furthermore, the fact that the cross breaks cylindrical symmetry could have been the source of some of the distortions, too. The distance between the cross and the trap center was also large, thus projecting the ions on the detector required a strong focusing step.

The proposed solution, which seemed to address all the above mentioned problems, was to install the position sensitive detector at a lower position than the 6-way cross. The work leading to this modification was however divided into a number of steps. First of all, an optimal set of voltages was simulated for the initial arrangement to be able to compare the effect of the new detector position with the best possible outcome of the previous one. Then, two lower detector positions were simulated and for each of them optimal transport voltages were obtained, determining the achievable resolving power. Finally, the detector position was changed to the one offering the largest resolving power and the initial and final positions were compared.

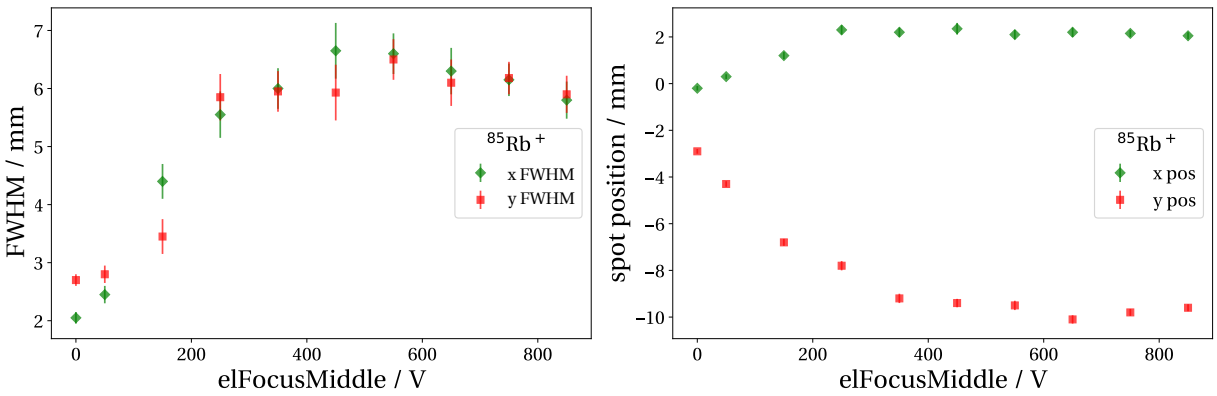

Figure 4.3: Variation of the spot size and position when changing the focusing voltage of the middle electrode of the einzel lens. The error bars for both the FWHM and the position information are obtained from the 2D-Gauß fit of the spot, for details see Sec. 4.2.

Optimization algorithm

To optimize the electrode voltages the SimIon [51] simulation software was used. The program solves the Poisson equation for a given set of boundary conditions (electrode voltages) using a Runge-Kutta 4th order algorithm and computes ion trajectories in the resulting potential distribution. It was combined with a simplex optimization algorithm, which works

with a simplex being the simplest volume in a N-dimensional parameter space. This N+1-dimensional construct is developed starting from an initial parameter choice, with the corresponding function's values. Among all N+1 points the algorithm calculates the "best" and "worst" point (i.e. yielding the largest and lowest value of the function, respectively) whereas the "best" is always kept for the next iteration step and the "worst" is always substituted by a new calculated, potentially "better" point and so on. This optimization algorithm, also known as hill-climbing or downhill search algorithm, is a medium-fast but very robust way of finding an extremum of a non-linear function. In our case it was initialized with a certain choice of transport voltages such that the transmission of the ions to the detector is as large as possible. Then the particle path to the detector was simulated and the optimization criterion was calculated. Then one voltage was changed, the simulation was run again and a new value of the criterion was determined. The process was repeated until an optimal solution was found. Since there can be many optimal solutions and there is a chance that the algorithm reaches only a local optimum the code was run several times with different starting potentials for all tested setups.

Magnetic field

One important aspect to consider was the magnetic field in which the detector would be lowered. Figure 4.4 shows the magnetic field along the beam line axis. The two colored arrows indicate alternative detector positions. The field strength is in both cases below the minimal requirement [12].

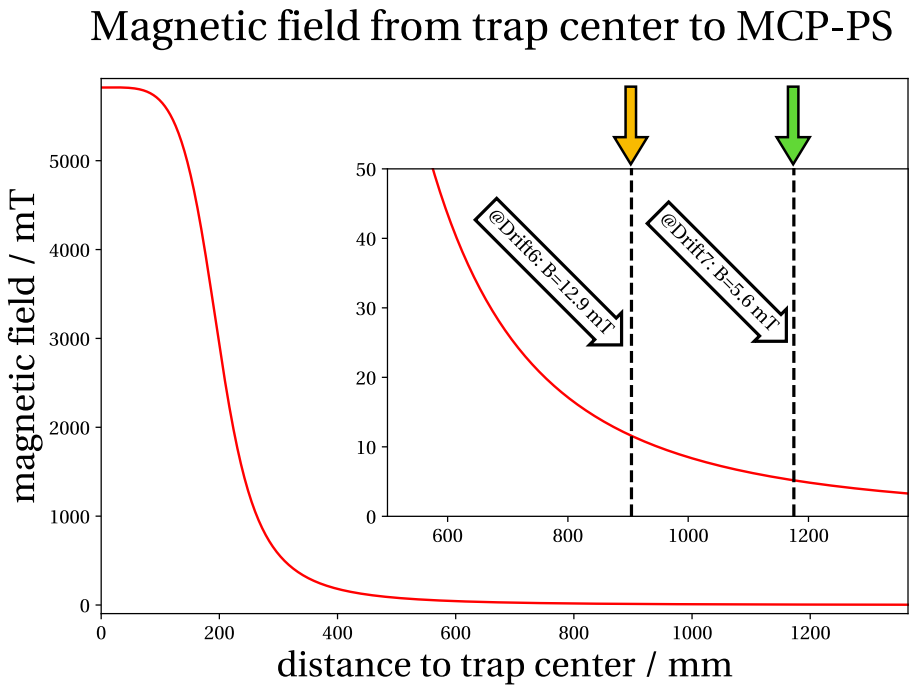

Figure 4.4: Magnetic field along the beam line axis highlighting the two alternative detector positions which were considered.

Simulation

The simulation of the beam trajectory (see Fig. 4.5) was performed for three configurations, all starting at the precision Penning trap, then passing through the magnetic field and the electrical fields of all drift tubes and the einzel lens, until the MCP-PS detector. The three configurations were:

- Configuration 0: starting condition as shown in Fig. 4.1
- Configuration 1: removing the einzel lens and the 6-way-cross, indicated by the green arrow in Fig. 4.1
- Configuration 2: removing the einzel lens, the 6-way-cross and drift tube 7; indicated by the yellow arrow in Fig 4.1

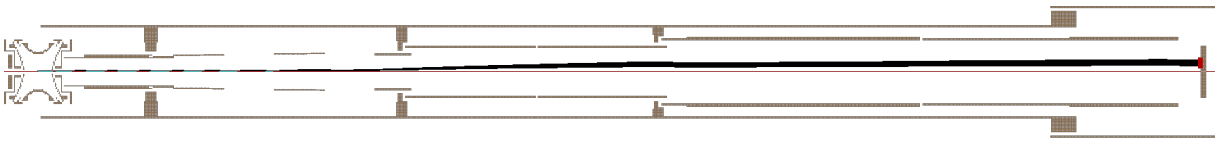

Figure 4.5: SimIon beam trajectory example for configuration 2 and sim#4 voltages (see Tab. 4.1).

For all simulations, the voltages of the available drift tubes and of the mesh on the position-sensitive detector were the free parameters. The initial ion distribution was chosen for singly charged ions with mass number $A = 100$. For the position a 3D Gaussian distribution at a point, which was (0.7 ± 0.2) mm away from the center of the trap, was chosen. This simulated a spot of ions excited on a magnetron radius within the expectation value of 0.7 mm. For the velocity, a 3D Gaussian distribution in direction of the circular motion at a speed of $(4 \pm 1)\,\frac{\mathrm{m}}{\mathrm{s}}$ (corresponding to a magnetron motion of ~ 1 kHz at a radius of 0.7 mm) was assumed. The initial velocity is small compared to the ejection from the trap, which accelerates the ions to $\sim 9 - 14\,\frac{\mathrm{km}}{\mathrm{s}}$ (for a singly charged ion with $A = 100$ and typical ejection voltages at ISOLTRAP of $V_{ejection} = 40 - 100$ V).

The optimization criterion Θ of the simulations was chosen as the resolution on the position sensitive detector. This is given by the ratio of the distance D between the spot corresponding to ions excited on a magnetron orbit and the center of the detector and the FWHM ΔR of the spot itself (see also Fig. 1.6):

$$\Theta = \frac{D}{\Delta R}\,. \tag{4.1}$$

The Tab. 4.1 shows different optimal voltage sets for all three configurations with the corresponding value of the optimization criterion Θ. Tests with the actual setup showed that a voltage difference between drift tubes 3 and 4, or 5 and 6, also leads to a steering of the beam,

probably due to a slight misalignment. To avoid this effect, the simulation forced equal voltages on the two neighboring electrodes of each pair. The following table summarizes results for selected simulations for configuration 0, 1 and 2.

Table 4.1: Local optimal potentials with the achieved value of the optimization criterion Θ (see Eq. (4.1)) given for configuration 0, 1 and 2.

Conf. 0	Drift1	Drift2	Drift3,4	Drift5,6	Drift7	E1,2,3	Mesh	Θ
Sim#4	-113.98	-396.28	-186.50	-222.48	-481.86	-725.84	-648.18	7.80
Sim#8	-138.01	-226.76	-151.94	-292.43	-628.01	-609.58	-611.86	6.68
Sim#11	-160.41	-208.53	-155.10	-300.18	-630.91	-602.75	-620.33	7.87

Conf. 1	Drift1	Drift2	Drift3,4	Drift5,6	Drift7	Mesh	Θ
Sim#1	-215.88	-234.20	-214.87	-475.17	-524.77	-420.38	3.81
Sim#2	-834.69	-499.32	-917.46	-499.82	-1000.05	-418.35	3.92
Sim#6	-944.89	-414.06	-868.13	-517.37	-933.29	-459.06	4.03

Conf. 2	Drift1	Drift2	Drift3,4	Drift5,6	Mesh	Θ
Sim#3	-152.17	-150.44	-321.01	-154.16	-557.85	7.00
Sim#4	-331.61	-174.93	-291.00	-311.54	-507.91	8.59
Sim#6	-287.71	-286.31	-57.53	-6021.31	-6009.41	4.74

Result of the simulations

The calculation time for each individual simulation, performed on a high-performance server cluster at the Max-Planck-Institute for Nuclear Physics (MPIK), was in the order of $2-8$ hrs. Comparing the three optimized configurations one can see the advantage of configuration 2, on the one hand over the original configuration due to the elimination of the 6-way cross distortions and slightly better results of the Θ-factor and on the other hand over configuration 1 with a clearly better resolution.

Figure 4.6 shows the calculated axial potential curves for the original configuration with the original voltages from a 2016 online run (red), optimized by hand, and two different optimization results (blue, green) for the same configuration. The differences are significant.

The following two plots show the improvement in practice after the simulated voltages are used. Figure 4.7 (left) displays the 2π phase clock of $^{85}Rb^{+}$-P1 spots with the original settings whereas Fig. 4.7 (right) shows the 2π phase clock of $^{85}Rb^{+}$-P1 spots with the original setup but the simulated voltages. The spots as well as the clock are now round and symmetric, usually with 1-2 mm spot FWHM and don't show strange deformation. Most importantly though, the settings are now *reproducible* and stable over time. For on-line beam times,

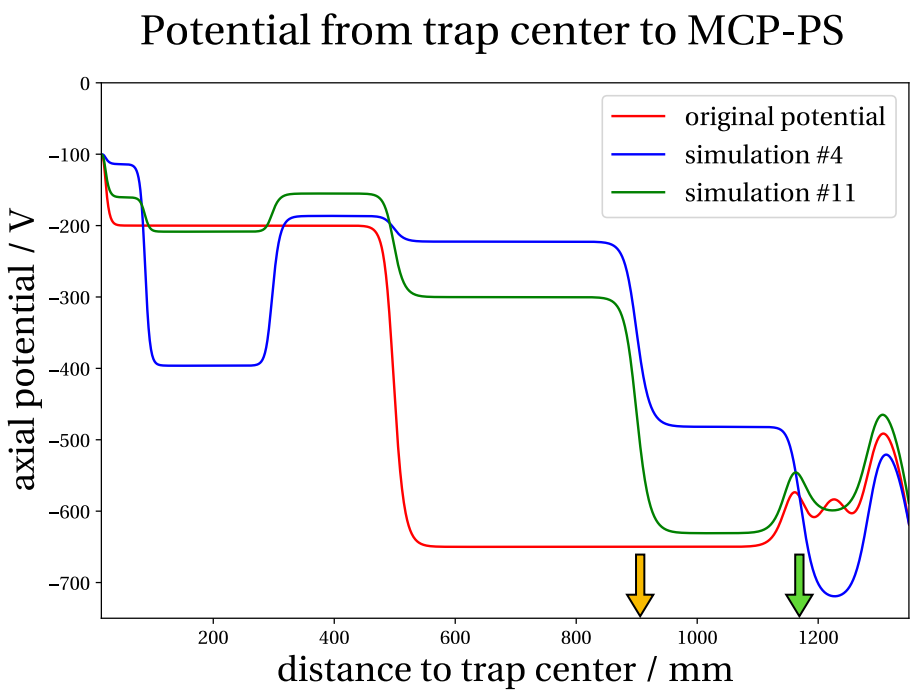

Figure 4.6: Comparison of the original potential curve (red) against the ones corresponding to simulated local optima (blue, green) for configuration 0.

when the available preparation time is limited to a few hours, the situation is even more drastic. A good example is shown in Fig. 4.8 for $^{127}Cd^{+}$, where the difference before and after the simulation studies and change of detector position is tremendous. Both runs displayed in this figure were part of the IS574 experiment. The data is taken from on-line the evaluation and should only demonstrate the improvement. In both cases, the phase accumulation time was $t_{acc} \approx 200\,ms$.

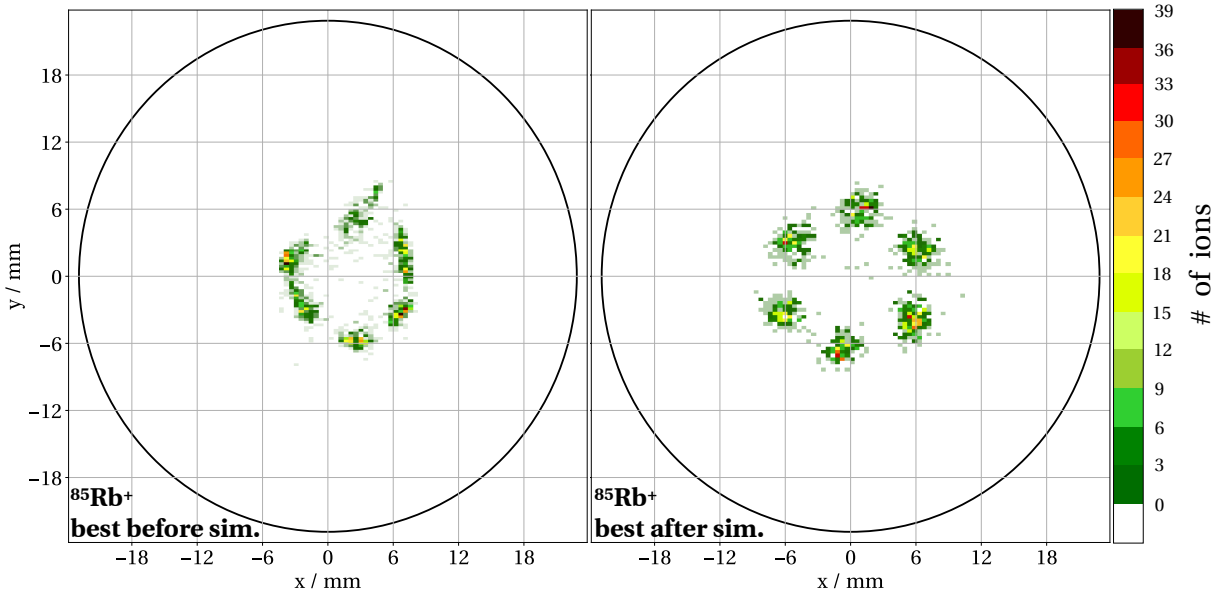

Figure 4.7: 2π phase clock (see Sec. 4.1) of $^{85}Rb^{+}$-P1 spots on the MCP-PS detector using the initial parameters (left, 2016) and the ones after the optimization using simulation studies (right, 2017).

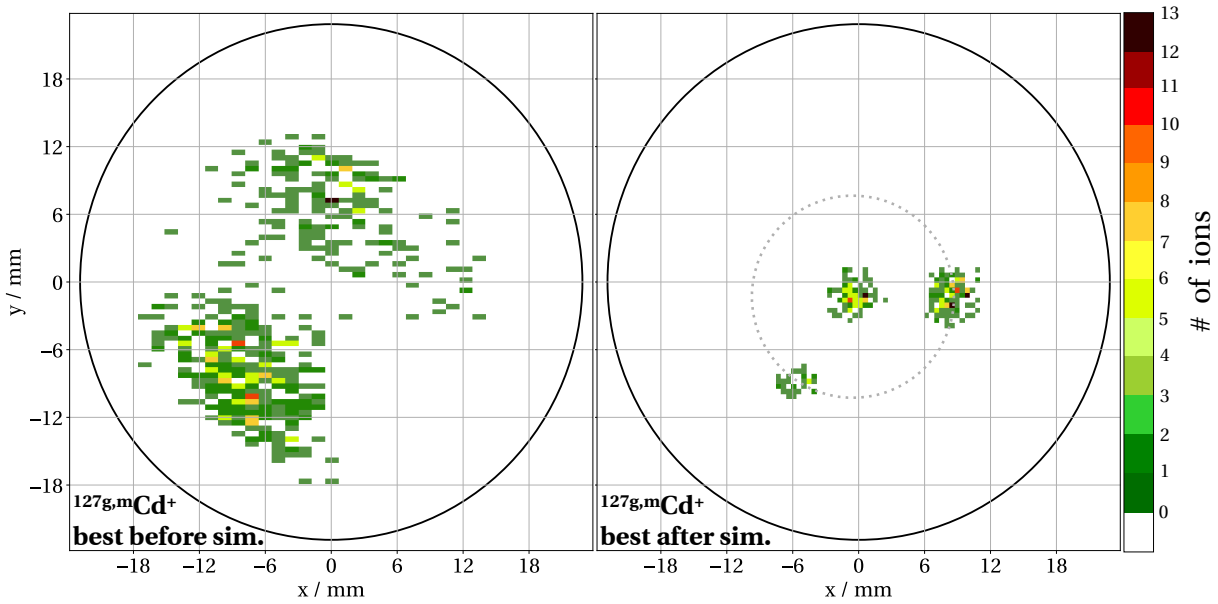

Figure 4.8: Ground and isomeric states of $^{127}Cd^{+}$-P2 spots before (left, 2016) and after the simulation studies and change of detector position (right, with center spot and ring to display the circular motion, 2017) as part of the IS574 experiment [52]. For details, see text and Tab. 4.2.

Table 4.2: ^{127gm}Cd properties. The mass excesses (ME) and half-lives are taken from [53], the yields given in number of ions per proton pulse (PP, see Sec. 2.2.2) are calculated from ISOLTRAP data. The half-life for ^{127m}Cd is interpolated.

Isotope	ME / keV	unc. / keV	$T_{1/2}$ / ms	unc. / ms	Yield / (ions/PP)
^{127g}Cd	-68747	12	320	20	~$0.2*10^5$
^{127m}Cd	-68472	8	200#	-	~$1.0*10^5$

4.2 Python-software development

In the initial tests of the PI-ICR technique, as well as during routine operation, a real-time LabVIEW reconstruction software from SHIPTRAP is being used. In an attempt to better understand event reconstruction, to potentially improve it and to include frequency-ratio calculation and mass determination, we programmed a new analysis software.

The new software is written in Python as it is a very easy and common language. It offers the possibility to implement the code into our current UI using the System Exec VI in LabVIEW or into the Python control system currently under development. Right now it is just used for a post-analysis, but it is planned to add it into the user interface (UI) as live-code.

Position sensitive detector

The position sensitive detector (MCP-PS) [54] consists of a mesh for field uniformity, two micro-channel plates (MCP) for converting the ion pulse in an electron avalanche and a 2D delay line arrangement which consists of a set of long, wrapped copper wires for both the X and Y direction (see Fig. 4.9).

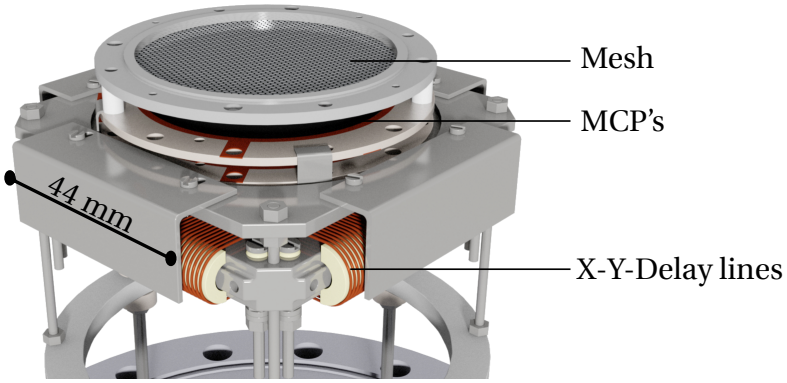

Figure 4.9: Drawing of the MCP-PS detector. On the top the mesh covers the two MCP's in Chevron configuration which are placed above the copper delay-line wires.

The whole detector, including the support rods connecting it to the flange, is less than 10 cm deep.

Imaging and reconstruction principle

An ion ejected onto the position sensitive detector first hits the MCP plates. The MCP converts the ion into an electron cloud accelerated to the wire detector (see Fig. 4.10). Electrons hitting the X and Y delay lines produce a short (~ 4 ns) negative pulse which propagates towards both its ends. The positive signal produced on the front MCP plate by the electron avalanche departing it, as well as the four signals from the delay lines, are amplified and converted to NIM pulses by a constant-fraction discriminator. They are then recorded by a time-to-digital converter (TDC), which is triggered by the ejection pulse of the ions from the

precision trap. With respect to this trigger, the TDC produced five sets of time stamps for the five sets of signals. The time stamps of the MCP are used to discriminate ion events from dark counts or switch noise. The ones from the delay lines are used to reconstruct the ion position. Hence, the detection system records 4 additional time stamps per ejection.

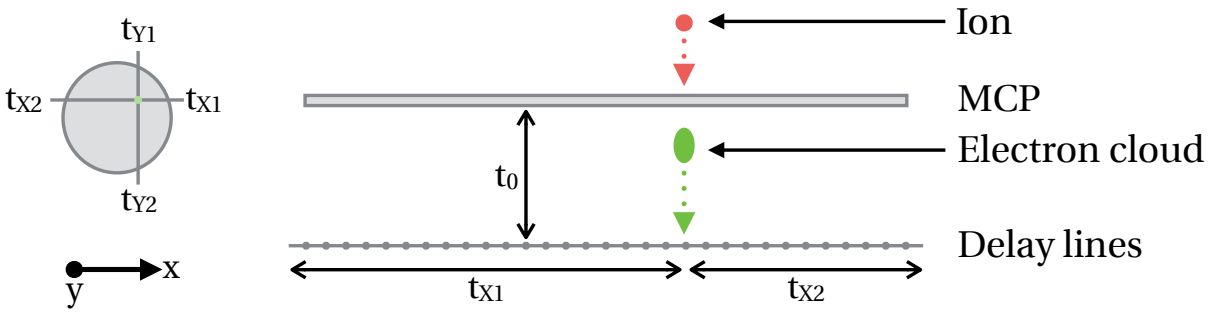

Figure 4.10: Schematic of the MCP-PS detector: MCP, X-Y-delay lines and highlight of the measured times.

In Tab. 4.3 one can see an example of time stamps for one ion ejection event. The first four lines represent the $X_1/X_2/Y_1/Y_2$ times respectively, where 1 and 2 express the two ends of a wire. The fifth line shows the measured MCP time stamps. All times are triggered on the ejection of the ions from the precision trap.

Table 4.3: Example of a raw data set for one single ejection event. The second column shows the number of measured events per line, while all following columns show times expressed in number of TDC channels. The first four lines represent the delay lines ($X_1/X_2/Y_1/Y_2$) and the fifth line represents the MCP. For this event three particles were detected.

line	# / line	t_1 / ch.	t_2 / ch.	t_3 / ch.
X_1	**3**	2506884	2523225	2527588
X_2	**3**	2507330	2523811	2528024
Y_1	**2**	2523484	2527820	
Y_2	**3**	2507075	2523547	2527776
MCP	**3**	2506339	2522740	2527029

In the example of Tab. 4.3 one delay line missed one event. Since the sum of the times in X or Y is conserved within a certain uncertainty, real events can be reconstructed even if one delay-line signal is lost. The algorithm checks all possible combinations per ejection event and compares the four delay-line times to a matching MCP time. The cut-off condition for an event on the detector, also known as time window, for the relative delay-line time $t_{nm} = t - t_{MCP}$ is:

$$0 \leq t_{nm} \leq t_{max} \tag{4.2}$$

with $n = [X_m, Y_m]$, $m = [1,2]$ and $t_{max} = t_{n1} + t_{n2}$.

Frequency calculation

After position reconstruction, the ion spots on the detector have to be fitted in order to determine their position and phase. For this purpose, a ROOT [46, 47] 2D maximum likelihood Gauss fit is used to calculate the most likely position on the detector. Furthermore the Hesse error matrix is computed to estimate the fit parameter uncertainty. According to

$$\phi_{\text{total}} = \phi_{\text{P1}} - \phi_{\text{P2}} \tag{4.3}$$

$$= \arctan2\left(X_{\text{P1}} - X_{\text{C}}, Y_{\text{P1}} - Y_{\text{C}}\right) - \arctan2\left(X_{\text{P2}} - X_{\text{C}}, Y_{\text{P2}} - Y_{\text{C}}\right), \tag{4.4}$$

the total angle ϕ_{total} between P1 and P2 can be calculated. Here, X/Y_i with $i \in$ [P1, P2, C] represent the most likely position from the fit whereas the function arctan2 is defined as

$$\text{arctan2} \quad : \quad E \quad \rightarrow \quad]-\pi, +\pi] \quad \text{or} \quad [-\pi, +\pi[\tag{4.5}$$

$$(x, y) \quad \mapsto \begin{cases} \arctan\left(\frac{y}{x}\right) & \text{for } x > 0 \\ \arctan\left(\frac{y}{x}\right) + \pi & \text{for } x < 0, y > 0 \\ \pm\pi & \text{for } x < 0, y = 0 \\ \arctan\left(\frac{y}{x}\right) - \pi & \text{for } x < 0, y < 0 \\ +\frac{\pi}{2} & \text{for } x = 0, y > 0 \\ -\frac{\pi}{2} & \text{for } x = 0, y < 0\,, \end{cases} \tag{4.6}$$

with $E := \mathbb{R} \setminus \{(0,0)\}$. This function "returns the angle, relative to the positive x-axis, of the line passing through the origin and the specific point" [55] and helps to calculate the phase no matter what position the spot is on. The function is also displayed in Fig. 4.11 for selected points on the unit circle starting at the point $P_0(x_0; y_0) = P_0(1;0)$ and moving counterclockwise. According to Eq. (1.19) the frequency can then be calculated.

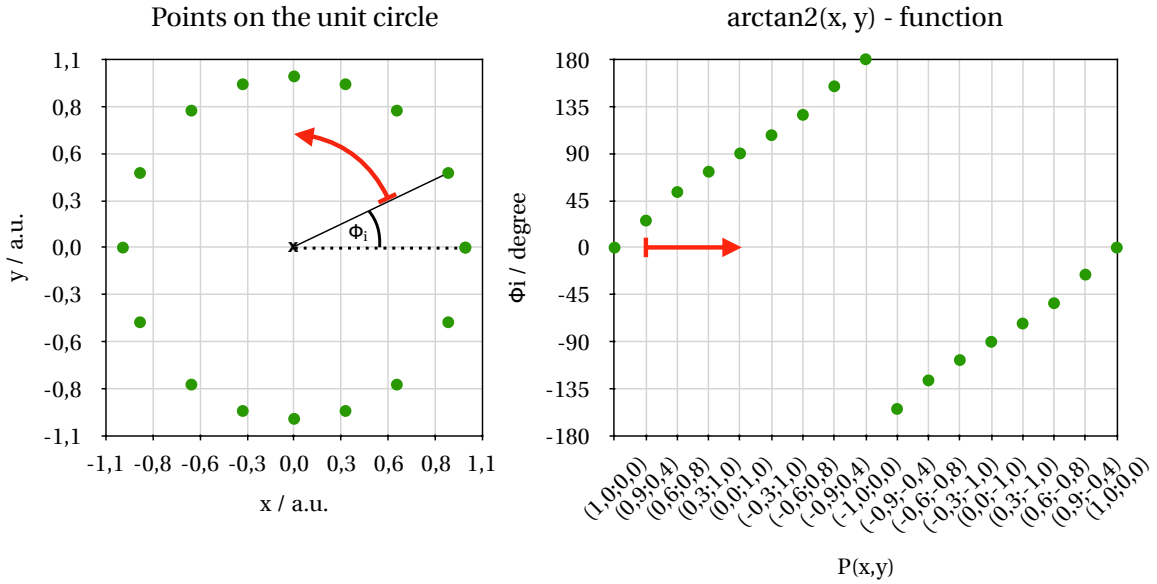

Figure 4.11: Selected points on the unit circle and arctan2(x,y) values for these points.

The software allows additional features:

- Fitting and calculating for several isotopes and files / runs at once.
- Z-class analysis: Hereby one selects only the events for which the number of ions per bunch is lower than a given one. This enables to control space charge effects inside the Penning trap. A typical maximal number of ions per event at ISOLTRAP is ≤ 5.
- Manual time-of-flight cuts and position cuts for the manual fit (see Fig. 4.12 left)
- Automated tool to reject counts corresponding to noise, random background or contaminants: The fitting of the spot position is iterative and starts by using the mean position on the detector as start value. At the second step it preserves the fit parameters of the previous fit as starting value for the next one. By reducing the fitted area on the detector to ~ 2.5 times the standard deviation of the previous fit, the software automatically rejects counts on the detector corresponding to noise, random background or low-yield contaminants. This step is repeated until the fit converges, typically 5 times.
- Automated tool to set the ToF window: The time-of-flight distribution of all reconstructed ions is iteratively fitted as it is explained in the previous point.

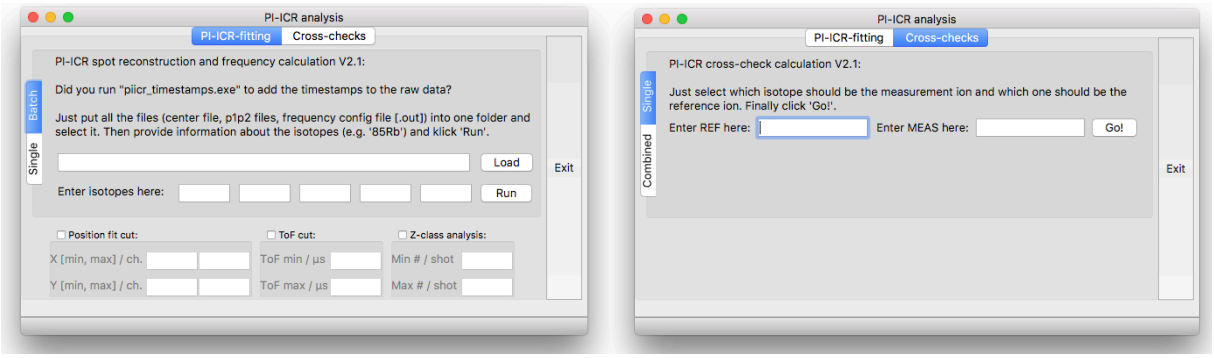

Figure 4.12: Python GUI for the PI-ICR-analysis software. The left picture shows the reconstruction and frequency calculation part and the right picture shows the mass determination part.

Mass calculation

The final analysis follows the article [45] and is similar to the one in Sec. 3.2. A frequency measurement of the atom of interest (= MEAS) is always combined with two frequency measurements of a reference ion (= REF) of well-known mass, one before and one after. This procedure allows calibrating the magnetic field and correcting the linear drift of the field during the measurement sequence. A set of measured frequency ratios is combined by the method of weighted averaging [48] and allows determining the atomic mass of the ion of interest by Eq. (1.17). The necessary mass information are derived from the database of the AME16 [49].

4.3 PI-ICR optimization procedure at ISOLTRAP

During the period of this thesis, a specific optimization procedure for the PI-ICR detection technique was established at ISOLTRAP and will be summarized in the following (and to cut out in Tab. 4.5). The procedure described here starts with a bunched ion cloud trapped in the preparation Penning trap.

1. The transport to the precision Penning trap (also called "upper trap") must be maximized and the injection angle must be minimized. On that account, all the electrodes of the precision trap are set on −10 V, which converts the trap into a lens for the ion bunch (so-called "shooting-through"-mode). The ions are then directly projected from the preparation Penning trap (also called "lower trap") onto the MCP-PS detector. One tunes, as a first step, the ion trajectory between the preparation and precision Penning traps because the latter one has a small ($ø_{UT} \approx 5$ mm) entry and exit hole. One thus optimizes the count rate on the MCP-PS detector by changing the voltages at the electrostatic lenses and steerers (see Fig. 4.2). The lenses with the largest effect on the ion cloud also in trapping mode are UT3, Retardation 1, and Retardation 2 (see Fig. 4.1) – being right in front of the upper trap – and the steerer with the largest effect is UT2X/Y, which is situated right before the UT3 lens.

2. The preparation Penning trap, filled with helium buffer gas for cooling, also has a small ($ø_{LT} = 1.5$ mm) exit hole, preventing the helium gas from spreading outside the lower trap and ensuring its resonant buffer gas cooling technique [36]. The ions exiting this trap towards the upper trap therefore must be on a magnetron radius smaller than the exit-hole radius in order not to collide with the wall. The reduction in magnetron radius is part of the radial cooling process, following a quadrupole excitation at the cyclotron frequency of the ion of interest. While still shooting through the electrodes of the upper trap, biased at −10 V, one scans the amplitude of the quadrupolar excitation and optimizes for the maximum number of ions (see Fig. 4.13). A proper cooling in the preparation trap would be reflected in an increase of the count-rate with the amplitude, until a plateau is reached, without further count-rate oscillations for larger amplitudes. One chooses an amplitude value slightly larger than the beginning of the plateau. Typical amplitudes for ^{85}Rb are in the order of $1-5$ V.

3. Further, the right upper-trap capture-pulse moment must be determined with the trap set back to capture mode (see Tab. 4.4). The ions are captured by switching the voltage of the lower end cap for about 40 μs to a voltage of −19 V. The end cap is switched back to trapping voltage when the ions are in the center of the trap. This moment must be set very accurately. If this happens too early/late, the ion cloud is accelerated in the axial direction and gains axial energy. The amount of axial energy can be measured with the MCP-PS detector by investigating the time-of-flight of the ions. To enhance the effect, the total trapping time is varied over a few periods of the axial motion. In case

of significant axial amplitude, the time of flight of the ions will oscillate with the axial frequency. In a summed ToF histogram, this essentially means that the ToF spread will increase for a non-optimal capture time. Figure 4.14 shows a capture delay scan while the ToF-spread from a trapping-time variation is recorded (the standard deviation of the summed histogram). The minimum is chosen and is, at ISOLTRAP for ^{85}Rb, typically on the order of $\sim 40\,\mu$s.

4. In the following two steps, the initial magnetron motion in the precision Penning trap is minimized to provide the same starting conditions for every repetition of the PI-ICR measurement (see also PI-ICR excitation scheme in Fig. 1.7). Hence and in contrary to ToF-ICR [9], the magnetron motion is minimized by scanning the moment when the excitation of the magnetron motion is applied (the so-called magnetron phase) and optimizing for maximal time of flight to the MCP-PS. A minimal time of flight to the detector would correspond to a large magnetron radius since radial energy is converted to axial energy in the magnetic-field gradient. Therefore a maximal time of flight corresponds to a minimal magnetron radius with minimal conversion in axial direction. To enhance this effect, the magnetron amplitude is increased (to typically $> 2.5\,$V) and the dipolar excitation at ν_+ in the PI-ICR excitation scheme is switched off ($\rightarrow \nu_+$-amplitude to 0 V). Figure 4.15 shows the magnetron phase scan where the maximal time of flight is chosen for PI-ICR and the minimum for ToF-ICR.

5. After the magnetron phase is locked, the amplitude of the upper trap magnetron excitation must be optimized to reduce the initial radius of the motion to zero. For the upper trap magnetron amplitude scan, the ν_+ excitation is still switched off to have only a pure magnetron to pure cyclotron conversion for every value of the magnetron amplitude. Again, the time of flight is measured for different magnetron amplitudes while choosing the amplitude with maximal time of flight as optimal for PI-ICR (see Fig. 4.16). A typical value of the PI-ICR magnetron amplitude for ^{85}Rb is $< 1\,$V.

6. Finally, the conversion pulse (also called "π-pulse") is optimized. In this case, as for the dipolar excitation of the magnetron motion, the amplitude leading to maximal time of flight will be determined. The scan is performed with both the optimized magnetron excitation (as described above) and the dipolar excitation at ν_+ switched on.

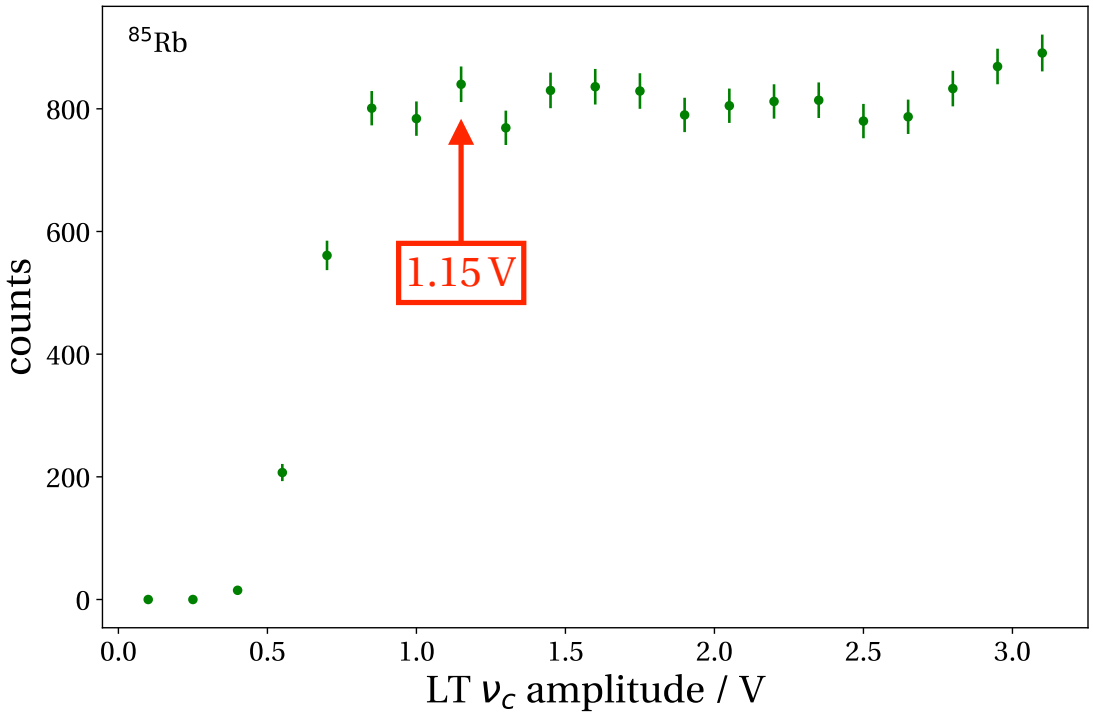

Figure 4.13: Lower trap cyclotron amplitude scan for ^{85}Rb taken during the IS490 beam time (see Sec. 4.4). The uncertainties are calculated as the square root of the number of counts. The red arrow indicates the chosen amplitude. For details, see text.

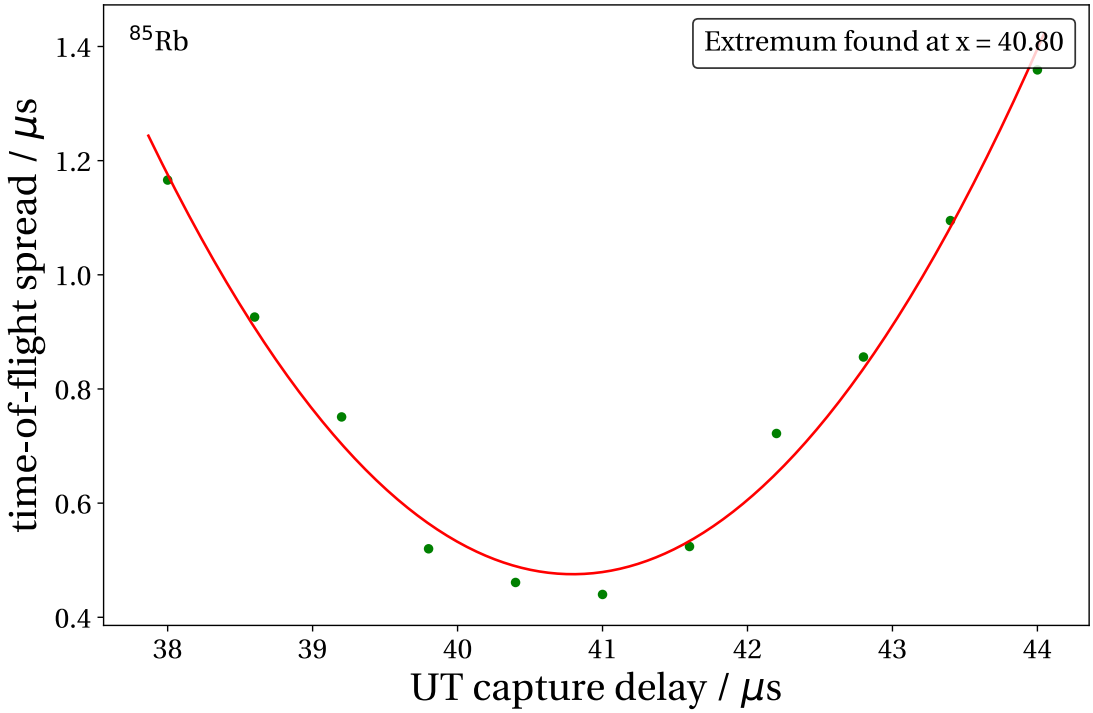

Figure 4.14: Upper trap capture delay scan with a polynomial fit for ^{85}Rb taken during the IS490 beam time (see Sec. 4.4). For details, see text.

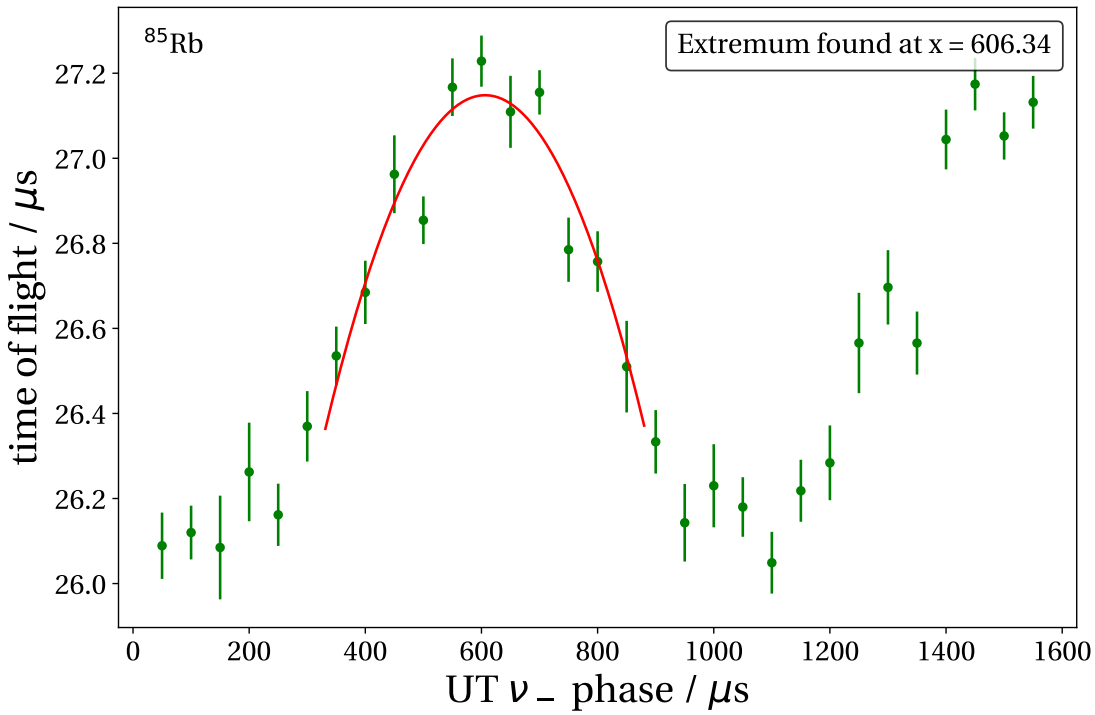

Figure 4.15: Upper trap magnetron phase scan with a polynomial fit for ^{85}Rb taken during the IS490 beam time (see Sec. 4.4). The uncertainties derive from the standard deviation of the time-of-flight distribution. For details, see text.

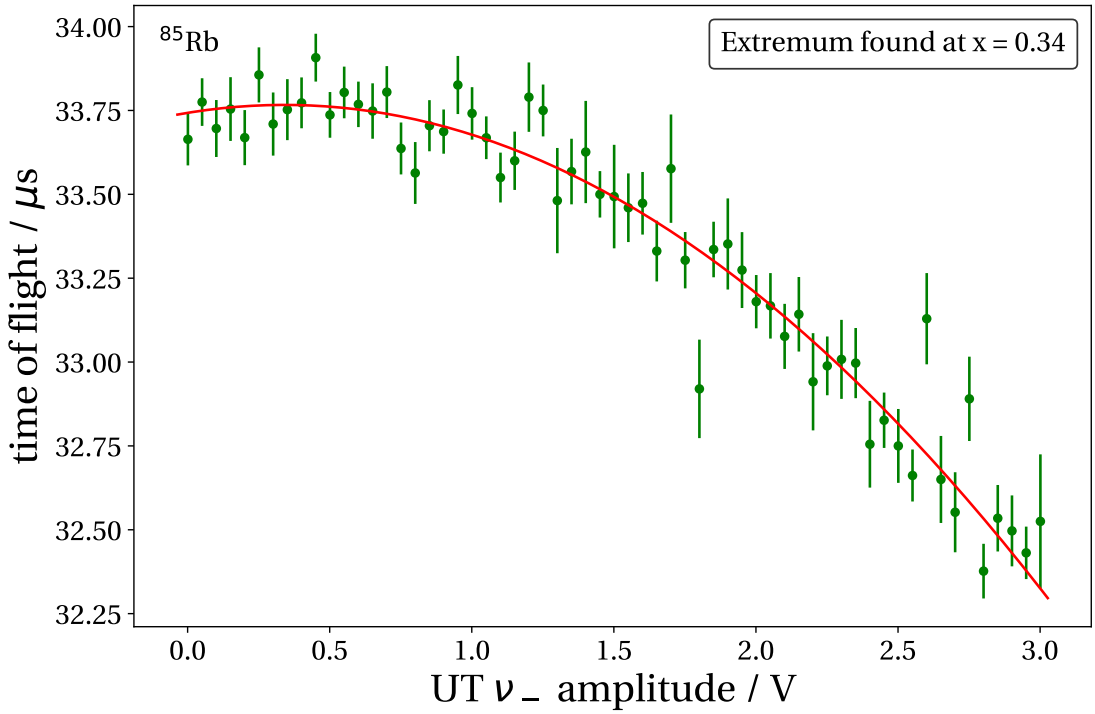

Figure 4.16: Upper trap magnetron amplitude scan with a polynomial fit for ^{85}Rb taken during the IS490 beam time (see Sec. 4.4). The uncertainties derive from the standard deviation of the time-of-flight distribution. For details, see text.

Name	Potential ToF-ICR / V	Potential PI-ICR / V
Lens UT3	485	
Retardation 1	130	
Retardation 2	44	
Lower correction tube	1.45406	
Lower end cap	-1.61125	
Lower correction ring	-8	
Upper trap ring	-10.119	
Upper correction ring	-8	
Upper end cap	-1.61125	
Upper correction tube	1.45406	
Upper trap extraction voltage	-19	-40
Drift 1	60	152.17
Drift 2	15	150.44
Drift 3	14	321.01
Drift 4	15	321.01
Drift 5	220	154.16
Drift 6	750	154.16
Mesh	558	
MCP-PS Ch.1	-2150	
MCP-PS Ch.2	300	

Table 4.4: Table with potential settings in capture mode at ISOLTRAP used for the IS490 beam time (see Sec. 4.4).

PI-ICR optimization

1. **Scan: LTcycAmp vs counts**
   → UT shooting through
2. **Scan: UTcapDelay (S2) vs EVA rec. time error**
   → minimize axial energy
   → update timing file
3. **Scan: UTmagPhase vs mean ToF**
   → increase ν_- amp (~2.5 V)
   → ν_+ amp to 0 V
   → update timing file
4. **Scan: UTmagAmp vs mean ToF**
   → ν_+ amp to 0 V
5. **Scan: UTpiPulseAmp vs UTpiPulseFreq**
   → mean ToF vs Amp
   → check spots

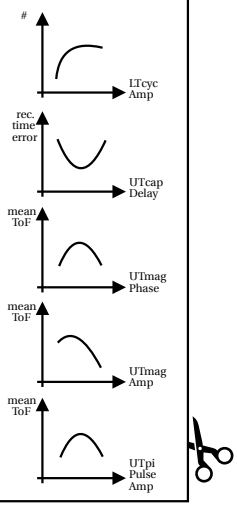

Table 4.5: Summary of the PI-ICR optimization at ISOLTRAP. For details, see text.

4.4 ^{88}Rb-^{88}Sr-Q-value

In May 2017 the PI-ICR technique was applied on-line for the first time in a test study to determine the well-known Q-value of the mass doublet ^{88}Rb-^{88}Sr. In this study the PI-ICR detection technique was compared to the ToF-ICR detection technique.

The uranium-carbide target was equipped with a neutron converter and a tantalum line. It was situated before the GPS separator and produced very clean Sr and Rb beams up to $A = 101$. Due to the high precision of the published mass values and the almost equal yield of ^{88}Sr and ^{88}Rb, the beam time was dedicated to the measurement of the ^{88}Rb-^{88}Sr-Q-value.

One sequence of irradiation (~ 30 min) was sufficient to produce the isotopes of interest in sufficient amounts in the target for an entire shift (= 8 hrs) of measurements. During the beam time, ToF-ICR resonances, especially using the Ramsey technique, as well as PI-ICR measurements were performed. The measuring order was ^{88}Rb-^{88}Sr as well as ^{88}Rb-^{88}Sr-^{85}Rb with ^{85}Rb from ISOLTRAP's offline source. The typical spot size and displacement are displayed in Fig. 4.17 where one observes both the center and the P2 spot (see Sec. 1.1.3) for ^{88}Rb.

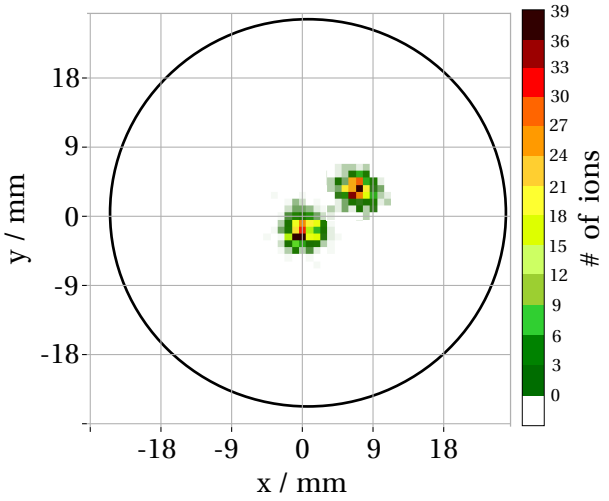

Figure 4.17: Typical spot size of ^{88}Rb during the IS490 beam time. Shown is a center spot (left) and a P2 spot (right).

Each measurement series used a certain choice of measurement parameters and included one measurement of the center spot for each isotope. This was then followed by alternating measurements of P1 and P2. This alternation was performed shot to shot to eliminate any chance of drifts between times when P1 or P2 were measured. As phase accumulation times 300 ms, 600 ms and 1 s were chosen. The second varied parameter was the amplitude of the dipole excitation at the modified cyclotron frequency. This changes the distance between the center spot and the spot of excited ions and therefore potentially the effect of the fringe field of the ion optics on the ions. As third parameter the initial overlap between the P1 and P2 spots on the detector was changed. Finally the initial phase of the π-pulse was varied.

Analysis

The literature values of the mass excesses and the half-lives for ^{88}Rb and ^{88}Sr are summarized in the following table.

Isotope	mass excess / keV	unc. / keV	$T_{1/2}$ / min	unc. / min
^{88}Rb	-82608.995	0.159	17.773	0.018
^{88}Sr	-87921.61793	0.00558	stable	stable

Table 4.6: Literature values of the mass excesses (taken from [49]) and the half-lives (taken from [56]) for ^{88}Rb and ^{88}Sr.

A summary of all measurements is shown in Fig. 4.18 and Tab. 4.7 where the difference between the AME16 [49] literature value and the measured masses of ^{88}Sr is shown. In all cases ^{88}Rb was taken as reference.

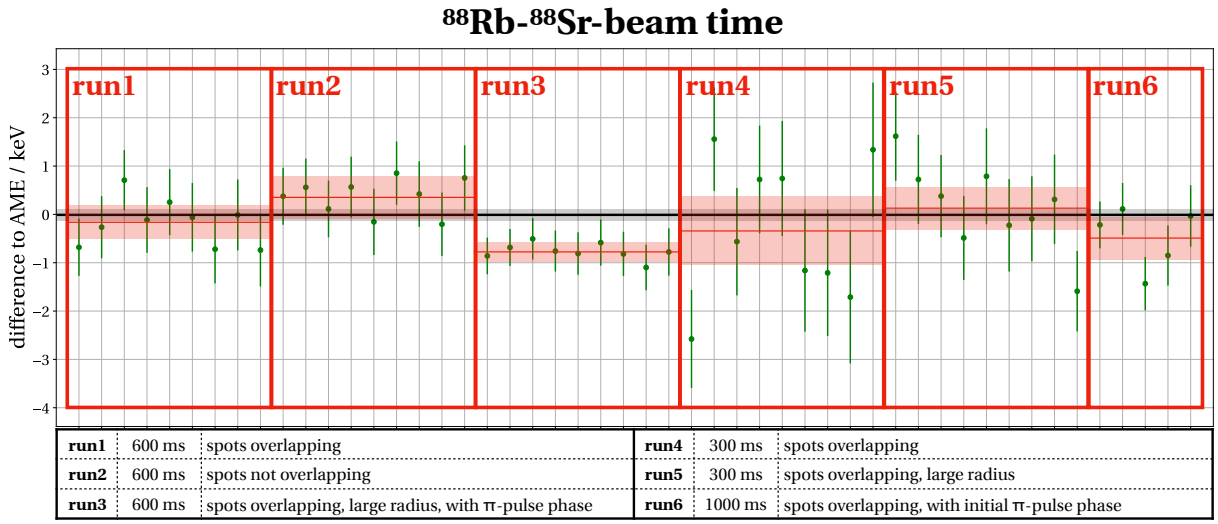

run1	600 ms	spots overlapping	**run4**	300 ms	spots overlapping
run2	600 ms	spots not overlapping	**run5**	300 ms	spots overlapping, large radius
run3	600 ms	spots overlapping, large radius, with π-pulse phase	**run6**	1000 ms	spots overlapping, with initial π-pulse phase

Figure 4.18: Difference between AME16 [49] and the PI-ICR measured masses of ^{88}Sr with ^{88}Rb as reference. Individual weighted averages [48] with uncertainties in red given for all runs. Varied parameters given in the plot.

Only an initial phase on the π-pulse was found to produce a systematic shift (see run 3 and 6). This could also be confirmed in offline cross-checks for ^{85}Rb-^{87}Rb as it is shown in Fig. 4.19 and is due to a DC offset introduced by the function generator before the beginning of the excitation, which then leads to a short transient pulse when the excitation begins and the offset is set to zero. All other parameters (the phase accumulation time, the amplitude of the dipole excitation at the modified cyclotron frequency and the initial overlap between the P1 and P2 spots on the detector) seem to have no statistically significant effect on the final frequency.

run#	Δ_{AME16} / keV	stat. unc. / keV	χ^2_{red}
1	-0.17	0.43	0.57
2	0.37	0.42	0.33
3	-0.76	0.37	0.14
4	-0.33	0.69	1.66
5	0.10	0.51	1.09
6	-0.49	-0.47	1.24
1+2+4+5	0.06	0.13	0.97

Table 4.7: Difference between AME16 [49] and the PI-ICR measured masses of ^{88}Sr with ^{88}Rb as reference, the statistical uncertainty and χ^2_{red} given for each individual run and the combined runs 1, 2, 4 and 5.

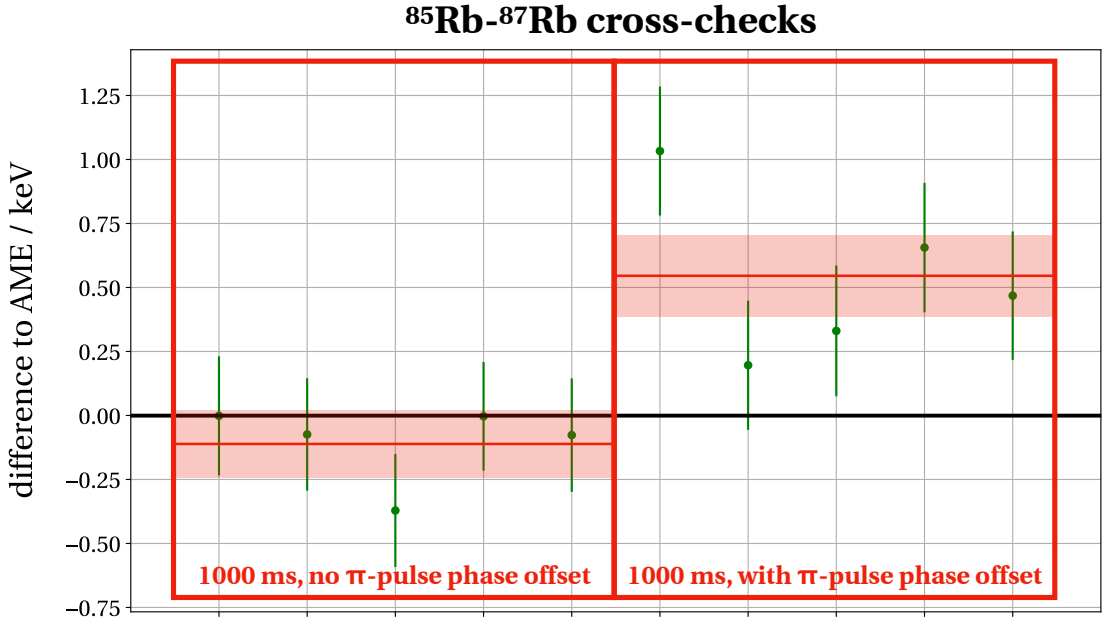

Figure 4.19: Difference between AME16 and the PI-ICR measured masses of ^{87}Rb with ^{85}Rb as reference. Individual weighted averages [48] with uncertainties in red given for both cases. Confirmed shift for measurements performed with an initial phase on the π-pulse.

Result

By restricting the ^{88}Rb-^{88}Sr data sets to the runs without an initial phase on the π-pulse the resulting Q-value is within one standard deviation from the AME16 and has an even lower uncertainty than the literature value reaching a precision of $< 1.5 \cdot 10^{-9}$. The final value is compared to the AME16 [49] value in Tab. 4.8 and will be published in a future article describing in detail the implementation of PI-ICR at ISOLTRAP.

Table 4.8: Q-value results of the β-decay pair ^{88}Rb/Sr in comparison to AME16 [49].

	β⁻-decay	Q-value / keV	unc. / keV
ISOLTRAP	^{88}Rb→^{88}Sr	-5312.68	0.13
AME16		-5312.62	0.16

The statistical precision of the PI-ICR measurements was for this run similar to the Ramsey measurements for the same phase-accumulation / excitation times and the same total measurement time (see Fig. 4.20). However the number of ions per file was kept approximately twice smaller for PI-ICR to conservatively reduce detector saturation and ion interaction effects.

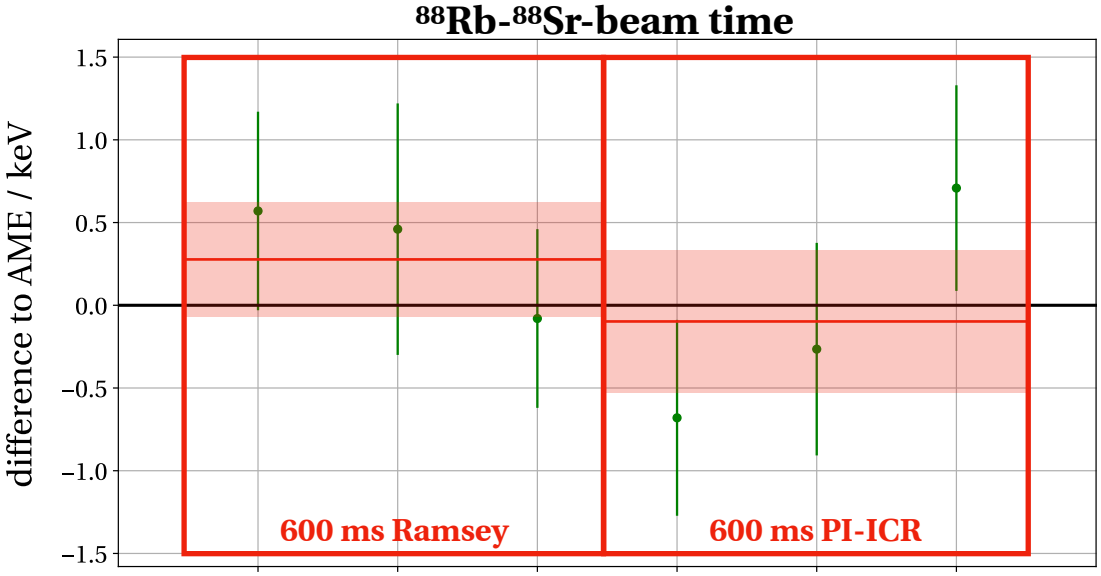

Figure 4.20: Difference to AME16 of the mass of ^{87}Rb determined with ^{85}Rb as reference. Individual weighted averages [48] with uncertainties in red given for both cases. The left points were taken with a Ramsey excitation (60-480-60 ms) and the right ones with PI-ICR (600 ms).

It remains to study how much one can gain in precision with respect to Ramsey with similar ion rate and by increasing the distance of the ion spot to the detector center. Furthermore one needs to investigate the ultimate accuracy of PI-ICR for measurements with reference ions further away in mass from the measurement ion. But already now one can conclude the clear advantage of PI-ICR over Ramsey in terms of precision per number of measured ions which definitely helps approaching isotopes with smaller production yields and shorter half-lives.

Summary and outlook

This thesis presented a characterization and improvement of the recently implemented Phase-Imaging Ion-Cyc- lotron-Resonance (PI-ICR) detection technique at the ISOLTRAP experiment, located at the ISOLDE facility at CERN, with the purpose of on-line high-precision and high-resolution mass spectrometry on short-lived nuclides.

Extensive simulation studies were performed and lead to a significant improvement of the phase-imaging resolution, especially during beam times with limited optimization time. Following the outcome of these simulations, the detector was moved out of a region of ion-optical distortions and closer to the center of the precision Penning trap, showing a dramatic improvement in the quality and reproducibility of the phase-imaging measurements. A new image reconstitution and analysis software for the MCP-PS detector was written in Python and ROOT and introduced in the framework of PI-ICR mass measurements. It significantly reduces the analysis time and has already been used in several on-line beam times during the period of this thesis. The state of the art in the field of time-of-flight ion-cyclotron-resonance measurements was illustrated through an analysis of on-line measurements of the mirror nuclei ^{21}Na/Ne and ^{23}Mg/Na using the Ramsey excitation pattern. The Q-values determined from this analysis play an important role for verifying the Conserved-Vector-Current hypothesis and for testing the unitarity of the CKM matrix. Finally, the results of a first high-precision, on-line measurement using the PI-ICR technique was presented, addressing the Q-value of the ^{88}Rb-^{88}Sr β-decay and proofing its successful implementation at ISOLTRAP. In addition, PI-ICR was used in further beam times in 2017, where in one its capability of close-lying isomer separation was successfully tested with the example of ^{127,129}Cd.

Following comparative measurements during the ^{88}Rb-^{88}Sr run between PI-ICR and Ramsey-TOF-ICR showing a similar PI-ICR statistical precision for almost half the number of measured ions, it remains to study how much one can gain in precision with respect to Ramsey with higher ion rates and by further optimizing the separation power. Furthermore, the reproducibility needs to be demonstrated in detail. In that respect, the phase relation among the excitation pulses is of high importance. For this purpose, a reference clock has to be implemented at ISOLTRAP. Finally, a PI-ICR ion-separation system, capable of exploiting at the achieved spatial separation, would be of high interest in order to produce clean singly isomeric beams.

Erklärung

Ich versichere, dass ich diese Arbeit selbstständig verfasst und keine anderen als die angegebenen Quellen und Hilfsmittel benutzt habe.

Genf, den 13ten September 2017,

_____

Jonas Karthein

Danksagung

Ich möchte mich herzlich bedanken

- bei Prof. Blaum für seine vielseitige Unterstützung und die Ermöglichung dieser Masterarbeit an einem der renomiertesten physikalischen Institute der Welt.
- bei Vladimir für die unglaubliche Hingabe als Betreuer dieser Arbeit und für seine Geduld beim Korrekturlesen.
- bei André, Dinko, Frank und Maxime für die vielen technischen, physikalischen sowie intellektuellen Diskussionen über Alles und Nichts.
- bei Caro für ihre aufmunternden Worte und ihr Verständnis für meine Arbeit fernab der Heimat.
- bei meiner Familie und meinen Freunden für die wichtige Unterstützung und regelmäßigen Besuche.

Ohne Euch wäre diese Arbeit so nicht möglich gewesen!

Bibliography

1. Eitel, G. *et al.* Position-sensitive ion detection in precision Penning trap mass spectrometry. *Nuclear Instruments and Methods in Physics Research Section A: Accelerators, Spectrometers, Detectors and Associated Equipment* **606,** 475–483 (2009).
2. Eliseev, S. *et al.* Phase-Imaging Ion-Cyclotron-Resonance Measurements for Short-Lived Nuclides. *Physical Review Letters* **110,** 082501 (8 2013).
3. Major, F. G., Gheorghe, V. N. & Werth, G. *Charged Particle Traps, Physics and Techniques of Charged Particle Confinement* (Springer, Berlin Heidelberg New York, 2005).
4. Blaum, K. & Sturm, S. *Stored Charged Particles* (Lecture notes, Universität Heidelberg, 2015/16).
5. Brown, L. S. & Gabrielse, G. Geonium theory: Physics of a single electron or ion in a Penning trap. *Reviews of Modern Physics* **58,** 233–311 (1 1986).
6. Bollen, G. *et al.* The accuracy of heavy-ion mass measurements using time of flight-ion cyclotron resonance in a Penning trap. *Journal of Applied Physics* **68,** 4355–4374 (1990).
7. Blaum, K. High-accuracy mass spectrometry with stored ions. *Physics Reports* **425,** 1–78 (2006).
8. *The Penning trap, Uni Mainz*; `http://wswww.physik.uni-mainz.de/werth/g_fak/penbew.gif`. Accessed: June 9^{th}, 2017.
9. Blaum, K. *et al.* Recent developments at ISOLTRAP: towards a relative mass accuracy of exotic nuclei below 10^8. *Journal of Physics B: Atomic, Molecular and Optical Physics* **36,** 921 (2003).
10. König, M. *et al.* Quadrupole excitation of stored ion motion at the true cyclotron frequency. *International Journal of Mass Spectrometry and Ion Processes* **142,** 95–116 (1995).
11. König, M. *Präzisionsmassenbestimmung instabiler Cäsium- und Bariumisotope in einer Penningfalle und Untersuchungen der Ionenbewegung bei azimutaler Quadrupolanregung*. PhD thesis (Universität Mainz, 1995).
12. Eliseev, S. *et al.* A phase-imaging technique for cyclotron-frequency measurements. *Applied Physics B* **114,** 107–128 (2014).
13. Bollen, G. *et al.* ISOLTRAP: a tandem Penning trap system for accurate on-line mass determination of short-lived isotopes. *Nuclear Instruments and Methods in Physics Research Section A: Accelerators, Spectrometers, Detectors and Associated Equipment* **368,** 675–697 (1996).

14. George, S. *et al.* Ramsey Method of Separated Oscillatory Fields for High-Precision Penning Trap Mass Spectrometry. *Physical Review Letters* **98,** 162501 (16 2007).

15. Eliseev, S. *et al.* Direct Measurement of the Mass Difference of ^{163}Ho and ^{163}Dy Solves the Q-Value Puzzle for the Neutrino Mass Determination. *Physical Review Letters* **115,** 062501 (6 2015).

16. Wolf, R. N. *et al.* Static-mirror ion capture and time focusing for electrostatic ion-beam traps and multi-reflection time-of-flight mass analyzers by use of an in-trap potential lift. *International Journal of Mass Spectrometry* **313,** 8–14 (2012).

17. Wienholtz, F. *et al.* Mass-selective ion ejection from multi-reflection time-of-flight devices via a pulsed in-trap lift. *International Journal of Mass Spectrometry* (2017).

18. Welker, A. *et al.* Submitted to. *Physical Review Letters* (2017).

19. Wolf, R. *et al.* On-line separation of short-lived nuclei by a multi-reflection time-of-flight device. *Nuclear Instruments and Methods in Physics Research Section A: Accelerators, Spectrometers, Detectors and Associated Equipment* **686,** 82–90 (2012).

20. Lunney, D. & behalf of the ISOLTRAP Collaboration), (Extending and refining the nuclear mass surface with ISOLTRAP. *Journal of Physics G: Nuclear and Particle Physics* **44,** 064008 (2017).

21. Wolf, R. *et al.* ISOLTRAP's multi-reflection time-of-flight mass separator/spectrometer. *International Journal of Mass Spectrometry* **349.** 100 years of Mass Spectrometry, 123–133 (2013).

22. *Map data ©2017 Google* ; `https://www.google.com/maps/`. Accessed: May 30th, 2017.

23. *Photograph by Maximilien Brice (CERN)* ; `https://cds.cern.ch/record/1295244`. Accessed: May 30th, 2017. Licence: CC-BY-SA-4.0, 2008.

24. Kugler, E. The ISOLDE facility. *Hyperfine Interactions* **129,** 23–42 (2000).

25. Catherall, R. *et al.* The ISOLDE facility. *Journal of Physics G: Nuclear and Particle Physics* **44,** 094002 (2017).

26. Borge, M. J. G. & Jonson, B. ISOLDE past, present and future. *Journal of Physics G: Nuclear and Particle Physics* **44,** 044011 (2017).

27. *ISOLDE website* ; `http://isolde.web.cern.ch/experimental-setups`. Accessed: July 11th, 2017.

28. Borge, M. & Blaum, K. Focus on Exotic Beams at ISOLDE: A Laboratory Portrait. `http://iopscience.iop.org/journal/0954-3899/page/ISOLDE%20laboratory%20portrait`. Accessed: September 7th, 2017.

29. Fedosseev, V. *et al.* Upgrade of the resonance ionization laser ion source at ISOLDE online isotope separation facility: New lasers and new ion beams a. *Review of Scientific Instruments* **83,** 02A903 (2012).

30. Mukherjee, M. *et al.* ISOLTRAP: An on-line Penning trap for mass spectrometry on short-lived nuclides. *The European Physical Journal A* **35,** 1–29 (2008).

31. Kreim, S. *et al.* Recent exploits of the ISOLTRAP mass spectrometer. *Nuclear Instruments and Methods in Physics Research Section B: Beam Interactions with Materials and Atoms* **317.** XVIth International Conference on ElectroMagnetic Isotope Separators and Techniques Related to their Applications, December 2–7, 2012 at Matsue, Japan, 492–500 (2013).

32. Savard, G. *et al.* A new cooling technique for heavy ions in a Penning trap. *Physics Letters A* **158,** 247–252 (1991).

33. Lunney, M. & Moore, R. Cooling of mass-separated beams using a radiofrequency quadrupole ion guide. *International Journal of Mass Spectrometry* **190–191,** 153–160 (1999).

34. Herfurth, F. *et al.* A linear radiofrequency ion trap for accumulation, bunching, and emittance improvement of radioactive ion beams. *Nuclear Instruments and Methods in Physics Research Section A: Accelerators, Spectrometers, Detectors and Associated Equipment* **469,** 254–275 (2001).

35. Raimbault-Hartmann, H. *et al.* A cylindrical Penning trap for capture, mass selective cooling, and bunching of radioactive ion beams. *Nuclear Instruments and Methods in Physics Research Section B: Beam Interactions with Materials and Atoms* **126.** International Conference on Electromagnetic Isotope Separators and Techniques Related to Their Applications, 378–382 (1997).

36. Rosenbusch, M. *et al.* A study of octupolar excitation for mass-selective centering in Penning traps. *International Journal of Mass Spectrometry* **314,** 6–12 (2012).

37. Gräff, G., Kalinowsky, H. & Traut, J. A direct determination of the proton electron mass ratio. *Zeitschrift für Physik A Atoms and Nuclei* **297,** 35–39 (1980).

38. Breitenfeldt, M. *Q-values of Mirror Transitions for fundamental interaction studies.* CERN-INTC-2014-038, INTC-P-410 (2014).

39. Bethe, H. A. & Bacher, R. F. Nuclear Physics A. Stationary States of Nuclei. *Review of Modern Physics* **8,** 82–229 (2 1936).

40. Weizsäcker, C. F. v. Zur Theorie der Kernmassen. *Zeitschrift für Physik* **96,** 431–458 (1935).

41. Hardy, J. C. & Towner, I. S. Superallowed $0^+ \rightarrow 0^+$ nuclear β decays: A new survey with precision tests of the conserved vector current hypothesis and the standard model. *Physical Review C* **79,** 055502 (5 2009).

42. Severijns, N. *et al.* $\mathcal{F}t$. *Physical Review C* **78,** 055501 (5 2008).

43. Patrignani, C. *et al.* Review of Particle Physics, 2016-2017. *Chinese Physics C* **40,** 100001 (2016).

44. Povh, B. *et al. Teilchen und Kerne: eine Einführung in die physikalischen Konzepte* (Springer-Verlag, 2006).

45. Kellerbauer, A. *et al.* From direct to absolute mass measurements: A study of the accuracy of ISOLTRAP. *The European Physical Journal D - Atomic, Molecular, Optical and Plasma Physics* **22,** 53–64 (2003).

46. Antcheva, I. *et al.* ROOT — A C++ framework for petabyte data storage, statistical analysis and visualization. *Computer Physics Communications* **180.** 40 YEARS OF CPC: A celebratory issue focused on quality software for high performance, grid and novel computing architectures, 2499–2512 (2009).

47. *ROOT website* ; `http://root.cern.ch`. Accessed: July 27^{th}, 2017.

48. Birge, R. T. The Calculation of Errors by the Method of Least Squares. *Physical Review* **40,** 207–227 (2 1932).

49. Huang, W. *et al.* The AME2016 atomic mass evaluation (I). Evaluation of input data; and adjustment procedures. *Chinese Physics C* **41,** 030002 (2017).

50. Welker, A. *A position sensitive detector for ISOLDE's high precision mass spectrometer ISOLTRAP.* PhD thesis (Technische Universität Dresden, 2017).

51. Manura, D. & Dahl, D. *SIMION*® Scientific Instrument Services, Inc. Ringoes, NJ 08551 (2008).

52. Kreim, S. *Precision Mass Measurements with ISOLTRAP to Study the Evolution of the N = 82 Shell Gap far from Stability* CERN-INTC-2013-022, INTC-P-382 (2013).

53. Audi, G. *et al.* The NUBASE2016 evaluation of nuclear properties. *Chinese physics C* **41,** 030001 (2017).

54. *Roentdek DLD40 manual* ; `http://roentdek.com/manuals/MCP%20Delay%20Line%20manual.pdf`. Accessed: July 28^{th}, 2017.

55. *Apple Numbers, trigonometric functions* ; `https://www.apple.com/mac/numbers/compatibility/functions.html#trigonometric`. Accessed: September 5^{th}, 2017.

56. McCutchan, E. & Sonzogni, A. Nuclear Data Sheets for A = 88. *Nuclear Data Sheets* **115,** 135–304.